ELSEVIER

Contents lists available at ScienceDirect

# **Extreme Mechanics Letters**

journal homepage: www.elsevier.com/locate/eml



# Stiffening multi-stable origami tubes by outward popping of creases



Zhongyuan Wo<sup>a</sup>, Evgueni T. Filipov<sup>a,b,\*</sup>

- <sup>a</sup> Deployable and Reconfigurable Structures Laboratory, Department of Civil and Environmental Engineering, University of Michigan, Ann Arbor, MI 48109, USA
- b Deployable and Reconfigurable Structures Laboratory, Department of Mechanical Engineering, University of Michigan, Ann Arbor, MI 48109, USA

# ARTICLE INFO

Article history:
Received 10 October 2022
Received in revised form 22 November 2022
Accepted 28 November 2022
Available online 5 December 2022

Keywords:
Origami tube
Conical Kresling
Pop-through
Stability
Tunable property

#### ABSTRACT

In this letter, we study the tunable stiffness and the multi-stability of corrugated tubes consisting of serially interconnected hexagonal frusta based on the Kresling origami pattern. Depending on the appropriate geometric designs, the corrugated origami tube either has straw-like behavior with an axial inversion and bending multi-stability, or has multiple axial stable states via a twisting motion. We focus on the latter category and reveal another stable "pop-up" configuration via outward popping of the valley creases. By switching among the three types of stable configurations, the corrugated tube can exhibit drastically different axial and bending stiffness. Moreover, the deformation mode can switch from twisting to inversion after the pop-up. To quantify the tunable mechanical properties, we employ an elasticity-based bar and hinge model and perform parametric studies that give insight on the relationships between geometry and mechanics. The results suggest that designs with a higher initial twisting angle and a lower initial slope will provide more significant stiffness and shape tuning, and that for specific designs the frustum stiffness can be increased by four orders of magnitude after pop-up. To validate the numerical results, we fabricate proof-of-concept origami frusta and corrugated tubes. These prototypes demonstrate the desired multi-stable behavior, the tunable stiffness, and mode switching deformations. These corrugated origami tubes have potential applications including mechanical devices of tunable properties, deployable structures, reconfigurable robotic components, and more.

 $\hbox{@\,}2022$  Elsevier Ltd. All rights reserved.

#### 1. Introduction

Structural stiffness is of great importance in many engineering applications, and the capability to manipulate the stiffness through a non-destructive way can offer tunable stiffness for novel application in mechanical metamaterials and adaptable structures [1]. Already, stiffness manipulation has been used for applications which are otherwise not achievable through conventional structures, such as the tunable robotic fish that can swim significantly faster [2], a tunable vibration isolator [3], the precise movement of octopus arms based on the localized stiffness tuning [4], minimally invasive surgery using a jamming mechanism with tunable stiffness [5], and a quadcopter frame that can soften during accidental collisions [6]. Among various means of creating tunable stiffness, multi-stable structures naturally offer different stiffness associated with the different stable configurations [7-10]. The recoverable deformation between stable states is often enabled by elastic buckling of confined beams and thin

E-mail address: filipov@umich.edu (E.T. Filipov).

shells [11–15]. Such local buckling behaviors help the multistable structures to find valuable applications, including reusable energy absorbers [13,16], the fast-encapsulating mechanism of flytraps [14], and reversible planar-to -3D transformations [17].

In addition to conceptual designs that have not been mass produced, there is a simple yet effective multi-stable mechanism that has been used in everyday life for decades: the flexible drinking straw [18,19]. The functional portion of the bendy straw is a corrugated cylindrical shell, which is composed of identical unit cells that are serially interconnected [20,21]. Each unit cell consists of two opposing frusta that are connected by a crease line (Fig. 1(A), the inset). In their most common realization, the bendy straw can morph and lock in both axial and bending deformations (Fig. 1(A)), allowing for continuous and variable change of orientations over the tube length. Those functions allow the corrugated tube to conform to different shapes [22], and transport fluids and gases [23,24]. By utilizing their unique shapemorphing and multi-stable features, researchers have deliberately created programmable and reusable energy absorbers [21,25] and a reconfigurable wire that can fit arbitrary 3D paths [22]. Owing to the wide spectrum of suitable applications, various research has been performed to better understand the underlying mechanics, including the influences of geometry [20], the

<sup>\*</sup> Corresponding author at: Deployable and Reconfigurable Structures Laboratory, Department of Civil and Environmental Engineering, University of Michigan, Ann Arbor, MI 48109, USA.

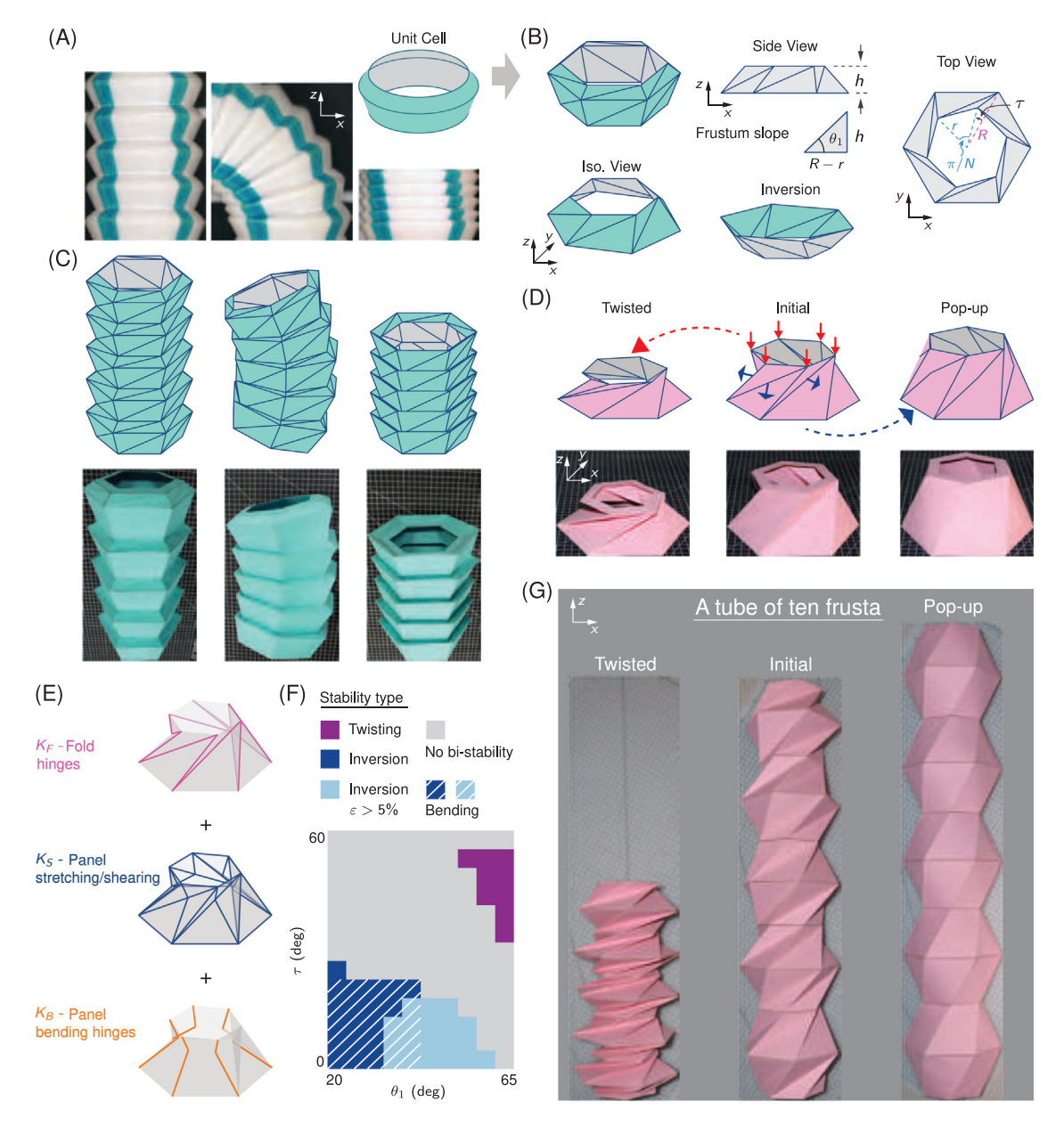


**Fig. 1.** Geometry of the Kresling cone and the corrugated tube. (A) A multi-stable straw in its three stable states. (B) An origami unit can be decomposed into Kresling frusta, for which the geometry can be described by the planar views. (C) A Kresling corrugated tube in its extended, bent, and collapsed states, illustrated by computer models (top row) and paper prototypes (bottom row). The two angles are  $\theta_1 = 30^\circ$ ,  $\tau = 0^\circ$  (top frusta) and  $\theta_1 = 70^\circ$ ,  $\tau = 0^\circ$  (bottom frusta) (D) A different Kresling frustum ( $\theta_1 = 65^\circ$ ,  $\tau = 50^\circ$ ) with a twisted, initial, and pop-up stable states shown by computer models (top row) and paper prototypes (bottom row). (E) Three components of the bar and hinge model shown on the single frustum. (F) The numerical predictions of stability for different geometry of the Kresling tube. (G) A ten-frusta corrugated tube showing three types of stable states ( $\theta_1 = 65^\circ$ ,  $\tau = 50^\circ$ ).

effects of pre-stress on the multi-stability [26], critical force of the constituent frustum [18,27], and the dynamics of pneumatic straws [28]. However, the curved surface makes it difficult to fabricate the exact shape as desired, and the conventional molding process for straw-like tubes introduces an uncertain amount of pre-stress [26]. Bernardes and Viollet thus introduced an origami design of the bendy straw that can be constructed without the casting process [29].

Origami, the ancient art of folding paper sheets into complex 3D geometries, has emerged as a predictable and programmable way to create multi-stable structures with tunable properties [30–36]. The Kresling origami [37] and its derivatives, have been extensively applied into the design of tubular mechanisms for the multi-stability, shape-morphing, and tunable stiffness. Multiple axial stable states allow the Kresling module to be a mechanical memory storage device [38], and the adjustable

stiffness can create a tunable vibration isolator [3]. By synthesizing the above three features, the Kresling origami demonstrated its use in achieving complex robotic motions with simple actuation sources, such as the multi-directional deformations [39,40], crawling robots [41-43], and a reconfigurable robotic arm with joint-link duality [44]. However, while Kresling-based designs can easily switch between different stable states via twisting motions, typically these tubes cannot bear axial loads. From the mechanics perspective, topology of the panels and creases are determined by the geometry and cannot be changed by deforming among different axial states. The deployment and retraction are guided by antisymmetric twisting motions with identical energy barriers, which implies that the deploying force will simultaneously increase with the load-bearing capacity. Zhai et al. [45] created a Kresling-inspired truss that can bear much higher uniaxial load, while the deployment is flexible. However, such design requires

bar members with asymmetric tension/compression behavior and it can only be realized in the form of truss structures rather than origami.

In this letter, we propose a versatile origami design of corrugated tubes consisting of conical Kresling units that shows drastically different multi-stability with different geometries. More importantly, these systems can be reconfigured into shapes with high load-bearing capacity. The corrugated tube is inspired by the bendy straw, but instead, the circular frusta are replaced by conical Kresling units to allow for easy fabrication to expand the space of programmable parameters. By tuning the geometry, the tube can behave either like a straw with axial and bending multi-stability, or as a tube that can switch among multiple stable states via a twisting motion. Furthermore, for the latter category, we revealed that another stable state, the pop-up, can be achieved through local snap-through buckling of panels around valley creases. After the snap-through, the Kresling module is turned into a pop-up dome shape with a topologically different arrangement of the panels and creases. As a result, crease folding and the twisting motion both become prohibited. The Kresling module gains high stiffness because the in-plane deformations of panels will be substantially involved in global deformations. Thus, axial and bending rigidity of the origami corrugated tube are both significantly increased by triggering the pop-up stable state of the Kresling units. This letter introduces and investigates the properties of the pop-up stability and is organized as follows: In Section 2, we introduce the geometric parameters of the Kresling corrugated tube and show different stability behaviors. Using a reduced-order numerical model, we capture and predict the multi-stability of inversion and twisting, as well as the pop-up (Section 3). We then present the underlying energy behaviors to understand why the pop-up process can be bi-stable. The shape change is quantified, and the subsequent tuning of the deformation mode is predicted and demonstrated. Section 4 investigates the influence of pop-up on the axial and bending stiffness. The pop-up and stiffness tuning are directly related to the origami pattern, and we perform parametric studies to explore how these behaviors are affected by geometric design. The pop-up multi-stability and the tunable stiffness are both demonstrated by paper prototypes. Finally, Section 5 provides a discussion on the main findings from this work and presents three conceptual applications based on the tunable properties.

# 2. Geometry, global multi-stability, and numerical model

The origami corrugated tube is inspired by the flexible drinking straw (Fig. 1(A)) and the Kresling origami pattern. A typical bendy straw is composed of identical units, where each unit (Fig. 1(A), the inset) consists of two frusta that are connected by a curved crease. A full inversion of the frustum can axially shorten the corrugated tube (Fig. 1(A), the right photo), while a partial inversion enables global rotation (Fig. 1(A), the middle photo). Our design started by mimicking the constituent circular frustum with a origami frustum (Fig. 1(B)), which is constructed using the conical Kresling pattern [46–49]. By eliminating the need to achieve a curved surface, the complicated molding process and associated pre-stress can be avoided. Here, we do not focus on realizing the straw-like behavior using the origami design, although it can be replicated with appropriate geometries (Fig. 1(C)). Instead, for another set of geometries, we find a "pop-up" stable state which offers tunable stiffness in both the axial and bending directions. This feature, to the best extent of our knowledge, has not been identified and analyzed in the existing literatures.

# 2.1. Geometry definition

The basic unit of the corrugated system presented in this letter is a single cell that is composed of two origami frusta (Fig. 1(B)). The circular cross-sections are approximated by regular polygons, and the curved shells are broken into flat panels connected by creases. For a single frustum (Fig. 1(B)), the crease pattern is inspired by a triangulated cone pattern that is reported to have multi-stability via twisting motions [46]. The frustum geometry is defined by five independent parameters: the radius of the circumscribed circle of the outer (R) and the inner (r) edges, the number of sides of the polygon (N), the relative twisting angle between the inner and outer polygons ( $\tau$ ), and the slant angle of the frustum ( $\theta_1$ ). In this letter, we choose the number of sides to be N=6 (hexagons), and the ratio R/r to be fixed at 1.55. The two angles  $\theta_1$  and  $\tau$ , will be systematically varied to explore the geometric influences on the pop-up stability and the subsequent stiffness change.

# 2.2. Different types of multi-stability

Two origami frusta are connected by creases to form a single unit cell, and a corrugated tube can be created by serially interconnecting several identical unit cells. With different frustum geometries, the origami tubes show different categories of multistable behavior. When the frustum is shallow and less twisted, i.e.,  $\theta_1$  and  $\tau$  are small, the tube can undergo a bi-stable inversion (Fig. 1(B)). We fabricate a prototype of a five-unit tube, using  $\theta_1=30^\circ$ ,  $\tau=0^\circ$  and  $\theta_1=70^\circ$ ,  $\tau=0^\circ$  for the top and bottom frusta in the unit cell, respectively. Those values are adapted from the measurements of commercial bendy straw [21], and the resulting corrugated tube can bend and shorten like a straw (Fig. 1(C), the bottom row). This multi-stable axial inversion and bending can be predicted (Fig. 1(C), the top row), using the reduced-order simulation tool that will be introduced in the following subsection.

On the other hand, when the frustum is steeper and more twisted, i.e.,  $\theta_1$  and  $\tau$  are greater, the origami frustum can collapse through a bi-stable twisting motion. As shown by the left part of Fig. 1(D), a frustum with  $\theta_1 = 65^{\circ}$ ,  $\tau = 50^{\circ}$  is collapsed to a more compact state via a twisting motion. Notice that, for a frustum in a corrugated tube, there exist two unique effects that cannot be captured by a single stand-alone frustum: (i) the confinement from neighboring frusta and (ii) the folding of creases that connect separate frusta. Therefore, extra strips of the same material are connected to the edges of the origami frustum to supplement those mechanical effects (photograph in Fig. 1(D)). During the twisting collapse, the folding of creases contributes to the axial displacement, while the in-plane deformations of the panels generate an energy barrier that separates two stable states [50]. The bi-stable twisting motion can be captured and predicted using an elastic truss model, in which the bars are arranged in the same manner as the crease network.

In addition to the crease folding and the in-plane panel deformations, another mechanism of deformable origami could be considered: the out-of-plane panel bending [51]. For instance, the panel bending is involved in the pop-through defects that create tunable stiffness in the Miura-ori tessellation [33]. Here we adopt a similar strategy to trigger a pop-up state that gains high stiffness. By applying forces and popping the valley creases (Fig. 1(D)), the frustum pops into a different mechanically stable state, which is referred as the *pop-up* state in the following discussions. The localized snap-through buckling is reversible because it does not involve plastic deformations of the panels (Section 3). After the pop-up, the frustum becomes stiffer by several orders of magnitude (Section 4), as the flexible twisting

motion is prohibited in the topologically different crease network. The tunable stiffness, combining with the shape-morphing capability, make the corrugated system a suitable candidate for several applications in different areas (Section 5). Based on the observations of the prototypes, once the system reaches the popup state, it will not switch back to the initial state under external axial or twisting forces.

#### 2.3. Numerical model and predictions

We use a bar and hinge model (Fig. 1(E)) to simulate the popup process, quantify the shape change, and to investigate the intrinsic tunable properties. The model treats deformable origami structures as pin-jointed truss structures with hinges. Recent advancements allow the model to simulate in-plane deformations and out-of-plane bending, as well as the crease folding, in both straight-crease origami [51–53] and curved-crease origami [54]. Based on elasticity, the simulation tool is capable of approximating nonlinear large-displacement responses rapidly and reliably, with much less convergence issues than the finite-element (FE) model. It has been carefully verified for various structures, and the predictions are in good agreement with those of analytical formulation, FE simulation, and experiments [20,54,55].

In the bar and hinge model, the folding of creases is represented by torsional springs defined along the crease lines, as illustrated in Fig. 1(E). The out-of-plane bending of panels is also represented using torsional springs that span across the panels, where the exact location will be discussed in Section 3. For this triangulated frustum (Fig. 1(B)), the in-plane deformations are captured by bars that outline the perimeter and along the same direction as the bending hinges. For a more in-depth discussion of the formulation and the usage of the model, please refer to [51,53].

The stiffness matrix of the system is comprised of contributions of the above three components, as well as a penalty term for preventing the contact between adjacent panels [53]. The stiffness of each of the three components is derived based on linear elasticity and the geometry. Here, we use a representative material with Young's modulus  $E=1.3\times10^9$ , Poisson's ratio  $\nu=0.3$ , and a normalized thickness  $t/R=4\times10^{-3}$ . We use arbitrary units and parameters of realistic relative magnitudes to discover the fundamental pop-up stability and the stiffness change. More details regarding the stiffness formulation, as well as the calibration with respect to finite-element results, can be found in Appendix A.

In order to understand the relationship between the geometry and the category of the multi-stable behaviors, we perform a parametric study with respect to the slant angle  $\theta_1$  and the twisting angle  $\tau$ . In other words, under a specific geometry, we explore whether a tube will exhibit the straw-like multi-stability of bending and inversion, or the twisting multi-stability. As compared to the finite-element method, the running time of the bar and hinge model is several orders of magnitude lower, making it an efficient yet sufficiently precise tool for exploring the parameters in a wide range. Here, we show the stability predictions for evenlydistributed  $\theta_1 \in [20^\circ, 65^\circ]$  and  $\tau \in [0^\circ, 60^\circ]$ , with a gap of five degrees (Fig. 1(F)). The numerical results match the conceptual observations of the paper prototypes, in which a combination of small  $\tau$  and  $\theta_1$  can provide a bi-stable inversion. Under an axial load, the origami frustum will be inverted to a nearly-mirrored configuration (Fig. 1(B), bottom left) when  $\tau$  is small (Fig. 1(F), bottom). More realistically, this inversion can only be observed with paper prototypes when  $\theta_1$  is also small because the strains increase with  $\theta_1$ . To demonstrate a realistic range where the paper prototypes only experience minor damage, i.e., the peak strain is less than 5% (the dark blue region). Regarding the bending simulation, we fix  $\theta_1=70^\circ$  and  $\tau=0^\circ$  for the bottom frustum of a unit, and only vary the two angles for the top frustum. We use a four-point bending test to check the bending stability of the corrugated tube [20], and a multi-stable bending can only occur with small  $\theta_1$  and  $\tau$  as well (Fig. 1(F)). The parameters of the bottom frustum can also have limited influence on the bending stability, but it will not change the trend with respect to the parameters of the top frustum [20,22].

As  $\theta_1$  and  $\tau$  increase, the axial response will change from inversion to twisting, and a combination of large  $\theta_1$  and  $\tau$  generate bi-stability (Fig. 1(F), top right). All other cases in-between will undergo a mono-stable twisting deformation, and the adjacent panels will come into contact before the strain energy reaches a local minimum.

A corrugated tube is constructed when the origami frusta shown in Fig. 1(D) are serially interconnected (Fig. 1G). Let m denote the number of frusta, there are up to  $3^m$  different states of the tube since each frustum has three stable states. However, we focus on three representative stable states of the tube as shown in Fig. 1G: from left to right: when all frusta stay at the twisted state, the initial state, and the pop-up state. Those states have different bending stiffness that will discussed in Section 4.

# 3. The pop-up deformation

In paper prototypes, we observe that the origami frustum can deform into and stay at a pop-up state (Fig. 1(D)). Using the bar and hinge model described in Section 2, we capture this bistability of the pop-up and understand the underlying energy behaviors, We then vary the two angles  $\theta_1$  and  $\tau$  to investigate the geometric influences on the stability and the shape change. A mode tuning of deformation, as well as a global bending deformation due to partial pop-up, will be discussed in Section 3.2.

# 3.1. Pop-up and the resulting shape change

For modeling the pop-up with the bar and hinge model, we need to determine the location of the bending hinges. Due to restriction of bending by adjacent panels, a parallelogram panel in an origami will bend along the short diagonal [56–59], especially in large deformations. Here, we observe a similar phenomenon for the triangular panels during the pop-up deformation (Fig. 2(A)). For the two adjacent triangular panels that are connected by a valley crease, there are two vertices that are not located on the connecting crease. After the pop-up (from (i) to (ii)), we draw a dashed line that connects those two vertices (Fig. 2(A), part (ii)). The two triangular panels bend with a single curvature over the dashed line (part (iii)), and such bending can be simplified and represented by the concentrated torsion of a hinge, within the bar and hinge model.

The simulation of the pop-up deformation with the bar and hinge model is shown in Fig. 2(B) for a frustum with  $\theta_1 = 50^\circ$ ,  $\tau = 35^\circ$ . In the planar pattern (Fig. 1(B)), each side of the frustum corresponds to a quadrilateral ABCD (Fig. 2(B)), in which one diagonal corresponds to the valley crease. We define bending hinges along the other diagonal to be able to capture the pop-up (Fig. 2(B), process (1)). The quadrilateral is thus divided into four triangles that intersect at a node E, and these intersecting nodes will be loaded with outward concentrated forces to trigger the snap-through buckling (Fig. 2(B), process (2)). Under an appropriate loading magnitude, the frustum will pop into a dome-like shape (Fig. 2(B), process (3)).

The pop-up state is a stable state, which indicates that the strain energy reaches a local minimum. This underlying energy behavior is captured in the bar and hinge simulation (Fig. 2(C)).

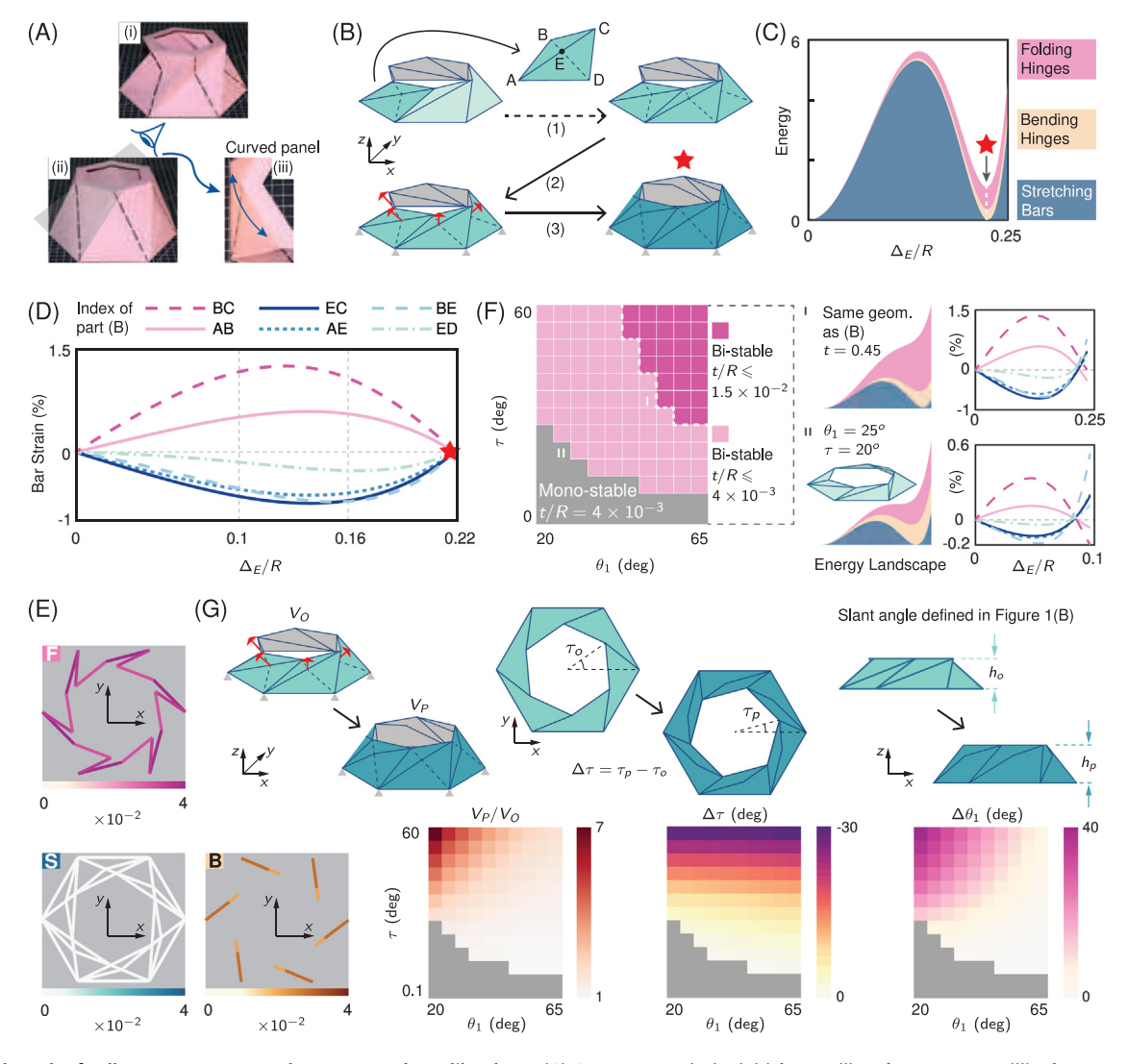


Fig. 2. Pop-through of valley creases converts the cone to a dome-like shape. (A) A paper cone in its initial state (i) and pop-up state (ii). The zoom-in photo (iii) shows the panel curvature after pop-up. (B) By placing a node on the valley crease, the pop-up process can be simulated by the bar and hinge model. (C) The energy landscape of a bi-stable pop-up process. (D) The bar strains experienced during the pop-up process. (E) The energy distribution at the pop-up state. The folding (F), stretching (S), and bending (B) energy plots are arranged counterclockwise. (F) Left: Numerical predictions of the pop-up stability with respect to the geometric parameters and the sheet thickness; Right: underlying energy behaviors of two mono-stable cases. (G) Shape change from the initial state to the pop-up state, including the enclosed volume (Left), the twisting angle (Middle), and the slant angle (Right).

There are three sources of strain energy that correspond to different mechanical deformations. The stretching strain energy first increases then decreases, while the bending and folding strain energies show monotonically increasing trends during the popup (Fig. 2(C)). Effectively, the total energy has a valley point that corresponds to the pop-up state. This bi-stable energy behavior is similar to the bi-stable bending of corrugated straws [20], where the in-plane strain energy is the only driving factor for bi-stability.

The pop-up deformation occurs without significant panel stretching as shown by the simulation results in Fig. 2(D), where the peak bar strains remain less than 1.5% during the pop-up. Because of these low strains, our physical prototypes do not experience visible damage after undergoing multiple cycles of the pop-up, i.e., remaining within the linear regime for construction paper [60]. Given that the deformation mode is axially symmetric, we only show the bar strains of one parallelogram, using the naming conventions of Fig. 2(B). The bar strains are plotted versus the normalized displacement  $\Delta_E/R$  of the intersecting node. At the pop-up state, the in-plane strain energy is negligible, as compared to the crease folding and sheet bending energies (Fig. 2(C), (E)).

From these analyses, we know that a pop-up deformation is bi-stable when the stretching energy dominates the process. Based on classical plate theory, the stretching energy is a linear function of the shell thickness t, while the bending energy is proportional to  $t^3$ . In the bar and hinge model, the folding energy and sheet bending energy are also both modeled as cubic functions of t (see Appendix A.1). Therefore, for the same geometry, the pop-up of frustum can be bi-stable with thinner sheets and mono-stable with thicker sheets. This relationship is confirmed by the parametric study shown in Fig. 2(F). Using a normalized thickness  $t/R = 4 \times 10^{-3}$ , the pop-up process is bi-stable for most geometries (the light pink and dark pink region). When the sheet thickness is roughly quadrupled, the bi-stable region shrinks to the top right corner (the dark pink region). Fig. 2(F) (part i) shows the energy behavior and bar strains for the frustum as in Fig. 2(B), (C), (D), but with higher thickness. During this mono-stable deformation, the bar strains show similar profiles as those of the thinner counterpart. However, the folding and bending energies occupy a greater portion, and there is no valley point in the total energy. A pop-up process can still be mono-stable with thin sheets  $(t/R = 4 \times 10^{-3})$ , and part ii of Fig. 2(F) shows an example

where the frustum geometry is  $\theta_1=25^\circ$ ,  $\tau=20^\circ$ . With the new geometry, the initial state is less twisted. The change in bar strains is similar, whereas the strain magnitude is significantly decreased from  $\sim 1.4\%$  to  $\sim 0.3\%$ . The stretching energy becomes less important and cannot counteract the increasing trends of the bending and folding energy. Therefore, the pop-up process is mono-stable.

The pop-up deformation converts a twisted Kresling frustum to a dome-like shape that has a different slant angle  $\theta_1$ , twisting angle  $\tau$ , and enclosed volume (Fig. 1(D)). These geometric changes are quantified using the simulation results (Fig. 2G). The frustum becomes a convex shape as the valley creases pop out, thus the enclosed volume is always increased. For most cases, the volume is elevated only slightly, while an extremely shallow and twisted frusta will see an sharp increase in enclosed volume by around seven times (Fig. 2G, the top-left corner of the first contour plot). After the pop-up, the frustum will become less twisted, as compared to the initial state. In other words, the relative twisting angle between the two polygons become smaller. As the initial  $\tau$  increases, the difference becomes more significant (Fig. 2G, the second contour plot). On the other hand, the slant angle, will become larger after the pop-up, i.e., the frustum becomes steeper (Fig. 2G, the third contour plot). Thus, a shallower and more twisted frustum gains a larger increase of the slant angle. As a summary, frusta with smaller  $\theta_1$  and  $\tau$  angles can result in more tunable systems that experience larger geometric shape change from the pop-up deformation.

# 3.2. Tunable deformation

We observe two phenomena that connect the pop-up with the multi-stable inversion and bending behaviors in Section 2. As we showed in Fig. 1(E), under an axial load, shallow and less twisted frusta can be inverted to a flipped configuration, while those that are steep and more twisted frustum experience a bi-stable twisting deformation. Those frusta in-between will undergo a mono-stable twisting deformation, and the adjacent panels will come into contact to prevent further axial displacement. Here, we set  $\theta_1 = 35^{\circ}$ ,  $\tau = 35^{\circ}$ , and while such a geometry does not have the classified twisting and inversion bi-stabilities, it can experience a bi-stable pop-up deformation. The mono-stable twisting deformation and the bi-stable pop-up deformation can be captured by both the bar and hinge model (Fig. 3(A)) and the paper prototype (Fig. 3(B)). After pop-up, when an axial load is applied to the top edge, the frustum can now also be inverted to a flipped configuration (Fig. 3(A), B, bottom row). Therefore, with certain geometries, a frustum can have two deformation modes under axial load: a mono-stable twisting or a bi-stable inversion after pop-up.

Besides the axial deformation, the bending stability can also be tuned by the pop-up. When we apply forces to all valley creases, a frustum is popped into a dome-like shape, where the top edge is still parallel to the bottom edge (Fig. 1(D)). However, the top edge becomes tilted with respect to the bottom edge when only one valley crease is popped (Fig. 3(C)). A relative rotation is thus created within a frustum, and a corrugated tube consisting of multiple tilted frusta will result in a globally rotated configuration. Here, we set  $\theta_1 = 65^{\circ}$ ,  $\tau = 50^{\circ}$  so this corrugated tube typically remains mono-stable for bending and cannot snap into different bent states like a bendy straw (Fig. 1(C), (E)). However, we simulate a corrugated tube consisting of sixty interconnected frusta, where each frustum is tilted by popping only one valley crease. This tube, which otherwise has no stable state under a bending moment, now turns into and stays at a knot-like shape (Fig. 3(D), top). When we only tilt a portion of the units in the middle, the tube will be turned into a stable L-shape (Fig. 3(D), bottom) This ability to selectively tilt the tube could potentially be used to fit target shapes, similar to what can be done with flexible straws [22].

#### 4. Tunable stiffness

The pop-up deformation not only provides the change of shape and stability, but it also allows for the stiffness tuning in the axial and bending directions. We observe the tunable stiffness with the paper prototypes, then quantify the stiffness tuning using the bar and hinge model. The following subsections describe the multi-step analysis used to explore stiffness tuning, as well as the underlying mechanics and geometric influence on these tunable behaviors.

# 4.1. Tunable axial stiffness

#### 4.1.1. Numerical predictions

The conical Kresling allows for tunable stiffness where the pop-up state is significantly stiffer than the initial state. A frustum with a large twisting angle  $\tau$  is flexible in its initial state that allows motion and deployment, but is stiff after reaching the pop-up state. Fig. 4(A) shows that, under the axial load from a plastic panel that weighs  $\sim 20$  g, a frustum ( $\sim 2.8$  g) collapses to a nearly-flat configuration via a twisting motion (from (i) to (ii)). However, after the pop-up (from (i) to (iii)), it support a masses of more than 1.5 kg without any visible deformation (iv).

This tunable axial stiffness can be captured using the bar and hinge model, and Fig. 4(B) illustrates the multi-step analysis for computing the axial stiffness. During pop-up step (step (1)), all the bottom nodes are fully restrained, and the valley creases are popped out by forces applied at the intersecting nodes (defined in Section 3.1). Next, the bottom nodes are released to slide (step (2)), and the pop-up frustum will settle into a slightly different configuration. Finally, using displacement control, the pop-up frustum is axially loaded to compute the stiffness (step (3)). Let  $\Delta$  denotes the axial displacement, then both the initial and pop-up states are compressed by  $\Delta = 1.3 \times 10^{-3} R$ . This displacement is small compared to the frustum dimensions so nonlinear behaviors can be neglected.

After the pop-up, the axial stiffness is increased by more than four orders of magnitude  $(K_P/K_O \approx 1.2 \times 10^4)$  for the geometry of  $\theta_1 = 50^\circ$ ,  $\tau = 60^\circ$ , as shown in Fig. 4(C). The rationale behind this drastic increase can be understood from the perspective of the fundamental mechanisms of the Kresling origami. The change of the energy distribution is plotted in Fig. 4(D) and E for the axial compression of the initial state and the pop-up state, respectively. For the initial state, the change of bending energy and in-plane energy in the panels are negligible, as compared to the crease folding energy (Fig. 4(D)). During axial compression in this initial state, the stiffness may vary due to the materials and fabrication process [61-64], but will remain flexible because only crease folding occurs. When popping the frustum into the pop-up state, the crease network is rearranged to be topologically different. As a consequence, the axial deformation mode requires stretching and shearing of the thin panels and thus a significantly higher amount of energy change occurs for the same applied displacement (Fig. 4(E)). Here, the crease folding and the panel bending energies are barely changed during the axial compression, while the in-plane energy of the panels increases substantially. Thus, the pop-up state is substantially stiffer than the initial state. Using a sensitivity analysis in Appendix B.1, we show that the value of the folding stiffness does not affect this conclusion.

The stiffness tunability strongly depends on the geometry of conical Kresling, specifically, the slant angle  $\theta_1$  and twisting angle  $\tau$ . The ratio of the pop-up stiffness to the initial stiffness is computed for those geometries that show bi-stable pop-up deformation (Fig. 4(F)). The parametric results indicate that, increasing the initial twisting angle  $\tau$ , or decreasing the slant angle  $\theta_1$ , can lead to a higher stiffness ratio. In other words, a shallower and

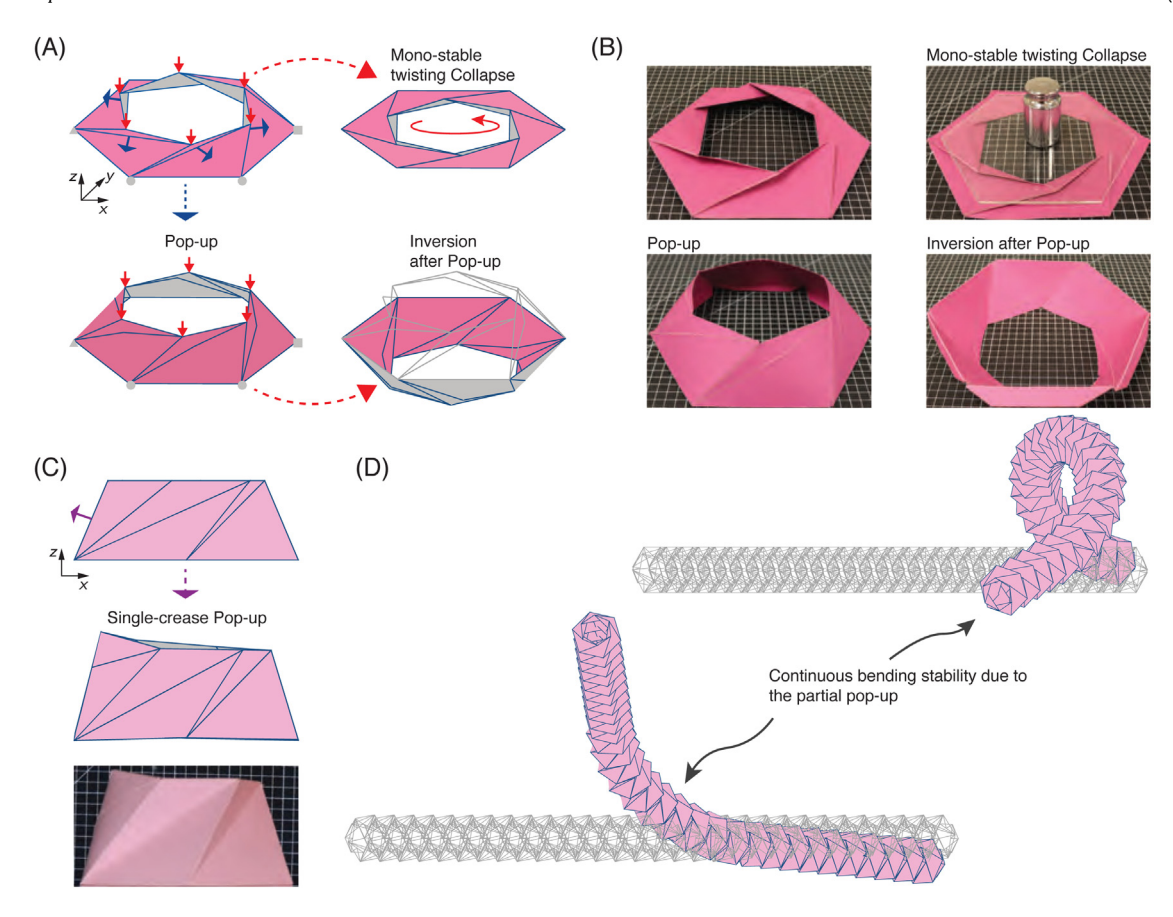


**Fig. 3.** Pop-through of valley creases enables the switching of deformation modes. (A) Under vertical loading, many Kresling frusta geometries are mono-stable and collapse via a twisting motion from their initial states. However, they can also be axially inverted after experiencing a pop-up deformation. (B) The axial mode switch demonstrated with a paper prototype. (C) By pop-through of only one crease, the Kresling frustum reaches a tilted state, which allows for continuously-changing orientations and bending-like multi-stability over the tube length, as shown in (D).

more twisted frustum offers more prominent stiffness tuning. This finding is correlated to the shape change in the pop-up (Fig. 2G), i.e., the stiffness sees a higher increase as the shape changes more.

In addition to the stiffness tunability, the actual stiffness can also be programmed by the two design angles ( $\tau$  and  $\theta$ ). The initial axial stiffness and the pop-up axial stiffness are plotted with respect to the twisting angle  $\tau$  for three slant angles  $\theta_1=40^\circ, 50^\circ, 60^\circ$  (Fig. 4G, H). All axial stiffness values are normalized by the maximum pop-up stiffness within the range of  $\tau \in [20^\circ, 60^\circ], \ \theta_1 \in [20^\circ, 65^\circ]$ . The axial stiffness of the initial state decreases when the twisting angle  $\tau$  increases, whereas the pop-up axial stiffness shows an increasing trend versus  $\tau$ . On the other hand, both the initial and the pop-up stiffness will increase with the slant angle  $\theta_1$ , i.e., when the frustum gets steeper.

# 4.1.2. Experimental verification of the axial stiffness tuning

The axial stiffness tuning is experimentally quantified using axial compression tests as described in detail in Appendix A.4. Here, we fabricate origami frusta of four geometries ( $\theta_1 \in \{50^\circ, 65^\circ\}$ ),  $\tau \in \{35^\circ, 50^\circ\}$ ), and compress each specimen at the initial state and the pop-up state (Fig. 5(A)). We run seven tests for each of the specimens, and Fig. 5(B) shows the average and the range of the loading responses. The compression distance is set to be small as compared to the frustum dimension, thus the loading responses are approximately linear. Based on linear regression of the experimental data, we compute the initial and pop-up stiffness, as well as the stiffness ratio (Fig. 5(C)). The experimentally-derived stiffness ratios are in good agreement with those of the bar and hinge model, and the largest relative error among the four geometries is 8.8%.

# 4.2. Tunable bending stiffness

A corrugated tube made of conical Kresling frusta will be multi-stable, where the number of stable states grow exponentially with the number of frusta. As shown in Fig. 1G, we focus on three representative states: where all frusta are configured to the twisted, initial, or pop-up states. In this section, we use eigenvalue analyses to compare the global bending stiffness, and cantilever tests to explore the bending isotropy.

To compare the tube bending stiffness at the three representative states, we perform an eigen analysis, where each eigenmode represents a unique deformation mode of the structure, and the associated eigenvalue is proportional to the total energy (kinetic and strain energy). A higher eigenvalue indicates a higher excitation energy and thus a higher stiffness for the corresponding mode. No boundary constraints are applied on the structure so the first six eigenmodes represent rigid body motions. We omit these modes and start the numbering at the seventh mode, i.e.,  $\lambda_3$  would be  $\lambda_9$  if those rigid-body modes are counted.

We set the tube geometry as  $\theta_1 = 65^\circ$ , and  $\tau = 50^\circ$ , and the global bending eigenmodes for each state are shown in Fig. 6(A). We select the first global bending mode, which effectively represents the most flexible way to bend the tube. By varying the initial twisting angle  $\tau$ , the eigenvalue corresponding to global bending is plotted for all three states (Fig. 6(B)). All eigenvalues are normalized by the maximum within the range of  $\tau \in [35^\circ, 55^\circ]$ . Frusta on the ends are reinforced to limit the localized eigenmodes, and as shown in Appendix B.2, these end reinforcements do not affect the global bending characteristics. Fig. 6(B) shows that the eigenvalue for global bending is highest

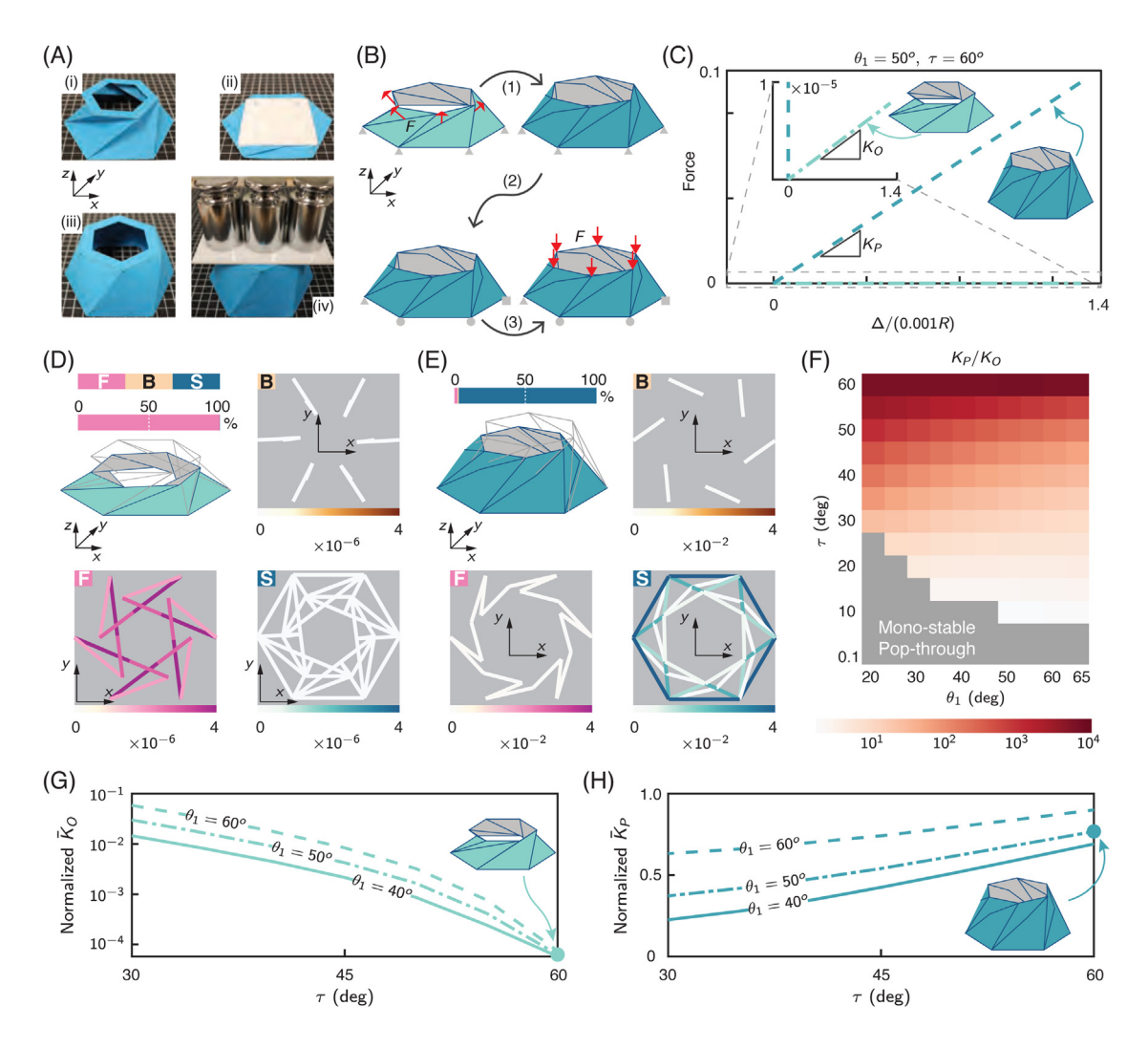


**Fig. 4.** The conical Kresling has a tunable axial stiffness. (A) The paper frustum can be collapsed by a thin plastic panel when it is in the initial state, but can support three calibration weights (1.5 kg) when in a pop-up state. (B) The simulation setup using the bar and hinge model. (C) Numerical predictions of the axial force-displacement ( $\Delta$ ) curves of the initial frustum and the pop-up frustum show that the structure is stiffer by more than ten thousand times. (D) The change of energy in different bending, folding, and stretching elements during the vertical loading for the initial frustum and (E) the pop-up frustum. (F) The ratio of the pop-up stiffness to the initial stiffness for different geometric parameters. (G) The normalized axial stiffness of the initial state ( $\tilde{K}_0$ ) and (H) the pop-up state ( $\tilde{K}_P$ ) vs. the twisting angle for three frustum slopes.

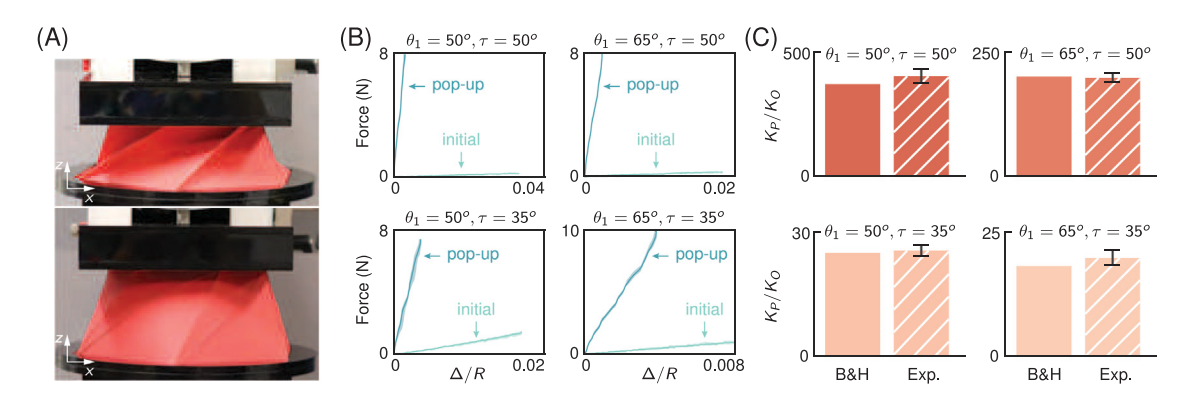


Fig. 5. Numerical predictions of the stiffness tuning are verified using axial compression tests. (A) A paper frustum being quasi-statically compressed in its initial state (top) and pop-up state (bottom). (B) The axial loading responses of paper frusta with four geometries. The solid lines are the averaged responses, and the shaded region denote the range of experimental data. (C) Comparison of the stiffness ratio between the bar and hinge model and the experimental results. The bars show one standard deviation of seven tests.

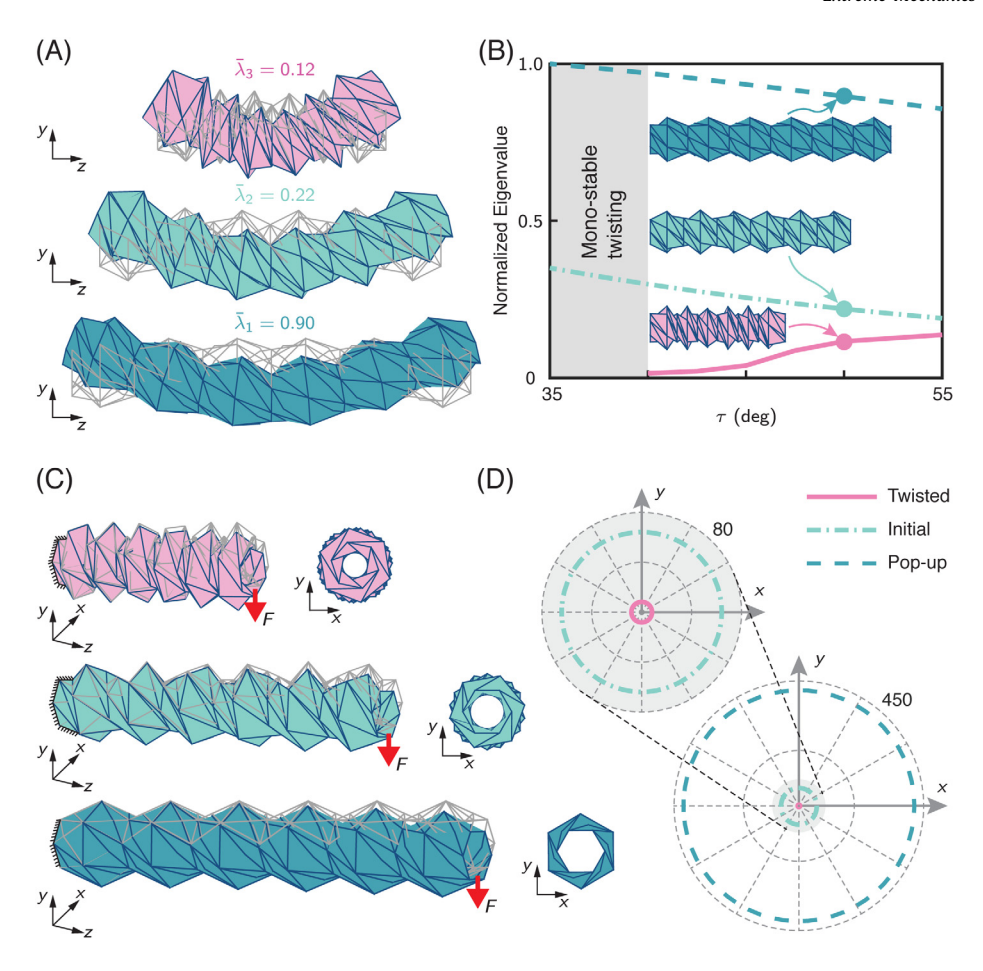


Fig. 6. Multi-stability of twisting and pop-up leads to tunable bending stiffness of the Kresling corrugated tube. (A) Deformation eigenmodes that correspond to the global bending of the twelve-frustum tube at its twisted state (top), initial state (middle), and pop-up state (bottom). (B) The normalized bending eigenvalue  $(\bar{\lambda})$  vs. the initial twisting angle for the three stable states. (C) Deformation of the corrugated tube when used as cantilevers at different stable configurations. The left end is fixed, and a uniform load is applied on the right end. The deformed shapes are scaled so the maximum displacement for each case is equal to the difference of the inner and the outer radius. (D) The equivalent section modulus (mm<sup>4</sup>) at the three stable states based on the cantilever test for loads in the X-Y plane represented as a polar plot. Here, the outer radius R is set to be 31 mm, and the section modulus is shown as distance from origin.

for the pop-up state, it is intermediate for the initial state, and is lowest for the twisted state.

The bending eigenvalues of both the initial state and the popup state decrease when the twisting angle  $\tau$  increases. On the other hand, the bending eigenvalues for the twisted state shows an increasing trend versus  $\tau$ . These opposing trends allow for designs where the bending stiffness can be highly tuned. For example, a tube with  $\tau=40^\circ$  will have normalized eigenvalues of 0.97, 0.30, 0.01 for the pop-up, initial, and twisted states respectively, while a tube with  $\tau=55^\circ$  will have normalized eigenvalues of 0.86, 0.19, 0.14 for the same three states.

We next use a cantilever test to explore the bending isotropy of the corrugated Kresling tube. The corrugated tube can find a suitable application as a reconfigurable cantilever with tunable stiffness. At the supported end, all nodes are fully fixed, whereas a total force of 1 is distributed on the other end of the tube (Fig. 6(C)). The cantilever stiffness is calculated as  $K = 1/\delta$ , where  $\delta$  is the maximum tip displacement. Based on the cantilever stiffness, we compute an equivalent section modulus (the second moment of area, I) for different directions orthogonal to the Z axis (Fig. 6(D)). Here, we use a fixed radius R of 31 mm. Using the section modulus for the bending comparison eliminates the effects of the tube length, thus giving a fair comparison among all three states. A convergence study shows that a tube with twelve frusta provides the equivalent section modulus that is within 0.1% of a tube with twenty frusta (see Appendix B.3). By deploying and

popping a tube from the twisted state, the section modulus can be increased by around fifty times.

Interestingly and beneficially, the section modulus is highly isotropic (Fig. 6(D)). Although the frusta are hexagonal, there are relative twists between the adjacent frusta that makes the cross-sections of the tube look like a circular shape, as depicted by the X–Y plane view (Fig. 6(C)). As a consequence, the tube is nearly-isotropic when used as a cantilever, meaning the loading response is consistent for all directions.

# 5. Discussion

#### 5.1. Key findings

Using the reduced-order model and paper prototypes, we explored and demonstrated the versatile shape-morphing and stiffness tuning of the conical Kresling tubes. In particular, the paper has demonstrated the following characteristics of the system.

**Geometrically governed multi-stability.** Each frustum unit of the Kresling tube can have a different multi-stable behavior that is governed by the pattern geometry, namely the twisting angle  $\tau$  and the slant angle  $\theta_1$ . Kresling frusta with a high twisting angle and a high slant angle possesses a twisting type bi-stability, while frusta with low twisting and slant angles can experience an inversion type bi-stability. A subset of Kresling geometries that

collapse via a twisting motions can also bend into a partially inverted state similar to the bending of a flexible drinking straw.

**Pop-up bi-stability.** The pop-up bi-stability occurs when the valley folds on the side of the Kresling frustum pop outward, and the two triangular panels become bent across a diagonal roughly perpendicular to the valley fold. An exploration on the geometric properties reveals that a more twisted frustum and one that is made of thinner sheets is more likely to be bistable for the pop-up deformation. When a Kresling frustum has pop-up deformations around the full perimeter, it can be axially inverted to a mirrored stable state. When only a single side of the frustum is popped out, the system undergoes a global bending-type deformation similar to a bent straw. As such, the pop-up bi-stability further enhances the range of deformed multi-stable configurations.

**Pop-up for stiffness tuning.**The pop-up bi-stability allows for tuning of both the axial and bending stiffness of the tube. As the pop-up distorts the frustum, the crease network is rearranged, and the flexible twisting motion becomes prohibited. The axial compression of a pop-up frustum thus primarily engages panel stretching rather than the crease folding, leading to a stiffness increase by up-to-four orders of magnitude. By varying the frustum geometry, we find that a shallower and more twisted frustum provides a more significant change in stiffness due to the pop-up. For certain geometries, the bending stiffness can be further tuned as the frustum can enter a twisted stable state that is more flexible than the initial state.

# 5.2. Conceptual applications

The conical Kresling system offers advanced shape-morphing and property tunability. Design of the Kresling geometry can change the multi-stability type and stiffness properties. Ultimately, each frustum could be designed individually to provide a different local behavior along the tube length. Based on the tunable properties and shape morphing, we propose the following three conceptual applications. We envision that the conical Kresling could be adapted for even more complicated scenarios.

**Tunable energy absorber.** When popped into the dome-like shape, the origami frustum gains a substantially higher resistance to axial compression. As compared to the initial state, the pop-up frustum is expected to generate significantly higher reaction forces during the quasi-static crushing and dissipate much more energy. A tunable energy absorber can be created, without using additional mechanisms to lock the system into a stiff and functional state [65]. We employ a finite-element model (ABAQUS/Explicit [66]) to simulate the crushing response, using the elastoplastic properties of a mild steel [67] and a twisting geometry ( $\theta_1 = 55^\circ$ ,  $\tau = 60^\circ$ ). We set the outer radius R = 31 mm and  $t/R = 4 \times 10^{-3}$ .

Under an axial compression, the initial frustum crushes to a nearly-flat configuration via a twisting motion that is guided by the crease pattern (Fig. 7(A)). The panels are barely stretched, sheared, or bent, and the majority of the axial resistance comes from the flexible folding at the creases. The reaction force curve increases linearly with the crushing distance and remains relatively low. With the material properties of a mild steel [67], the initial frustum absorbs 0.76 J. The pop-up frustum, however, crushes similar to a conventional prismatic crash-box type energy absorber [67] and generates substantially higher reaction forces. When the pop-up frustum is compressed, the crushing results in more panel deformations and material yielding (the insets of Fig. 7(A)). The pop-up crushes with a substantially higher force plateau and absorbs significantly more impact energy. For this

tube design, the pop-up absorbs 7.5 J, showing a roughly tenfold increase as compared to the initial frustum.

Deployable traffic cone. Given the conical shape and large geometric reconfigurability, the Kresling frustum can be used to construct practical deployable structures such as a traffic cone that allows for compact storage. As shown in Fig. 7(B), three frusta with shrinking radii are axially stacked to mimic a cone. The frustum geometry is set to be  $\theta_1 = 65^{\circ}$ ,  $\tau = 40^{\circ}$  such that the twisted state is nearly-flat when collapsed. Here, we set the outer radius of the bottom unit to R = 120 mm, and twisted state is about 46 mm high. By pulling up, all frusta switch back to their initial state and the cone deploys to about 222 mm. In this state, the structure remains flexible and can be readily collapsed back. As an alternative, the valley creases can be pushed into the pop-up state which increases the axial load-bearing capacity and ensures that the structure will not collapse back to a stowed state. At the pop-up state, the cone height is 271 mm, showing a nearly-six times increase from the twisted state. The traffic cone is reusable since the deployment and the pop-up will not engage plastic deformations.

Reconfigurable robotic arm. Another potential application of the system is to create robotic arms with localized tuning of bending stiffness. Soft robotic arms can maneuver effectively in complicated environments because they can undergo large bending deformations without failure [68]. However, continuum system made of soft material have infinite degrees of freedom (DOFs), causing overly flexible systems and increased complexity of achieving accurate motion control [44]. On the other hand, traditional robotic arms made of rigid links and flexible joints allow for precise movement but poor conformability. Utilizing the popup deformation which tunes the bending stiffness, one can build a reconfigurable robotic arm that switches between a compliant mode and a joint-link mode [44]. Here, we illustrate the idea using a tube of twenty four frusta (Fig. 7(C)). When every frustum is configured to be in a twisted state, the tube is flexible allowing for compliant deformations that can conform to a circular shape. The structure can then be transformed into a joint-link mechanism where some frusta stay in the twisted state to serve as a flexible joint, while others are popped up to form rigid links. According to the cantilever analysis in Section 4.2, there is a more-than-fifty times difference of bending stiffness between the flexible joint and the rigid links. This concept for a reconfigurable robotic arm can allow for versatile maneuverability and transformation into a more controllable joint-link system.

# 6. Concluding remarks

In this letter, we explored corrugated tubes made of conical Kresling origami. These offer a wide range of multi-stable deformations and tunable stiffness characteristics. By applying concentrated forces to pop the valley creases outward, an initially twisted unit can be "popped into" a unique dome-like state. We use an elasticity-based model to investigate the pop-up behavior, its shape-morphing characteristics, and the stiffness tuning that it offers. Proof-of-concept prototypes were fabricated from construction paper and are used to demonstrate the predicted bi-stability, as well as the subsequent stiffness change. Finally, we propose and discuss three potential applications, corresponding to the axial tunable response, the shape-morphing, and the tunable bending stiffness.

This work focuses on the identification of stability, understanding of the underlying mechanics, and quantification of the associated stiffness tuning. Future work on the system could explore the practical realization and usage of the tunability. For example, the tube could be appropriately sealed and pneumatically actuated to achieve state transitions. Moreover, studies

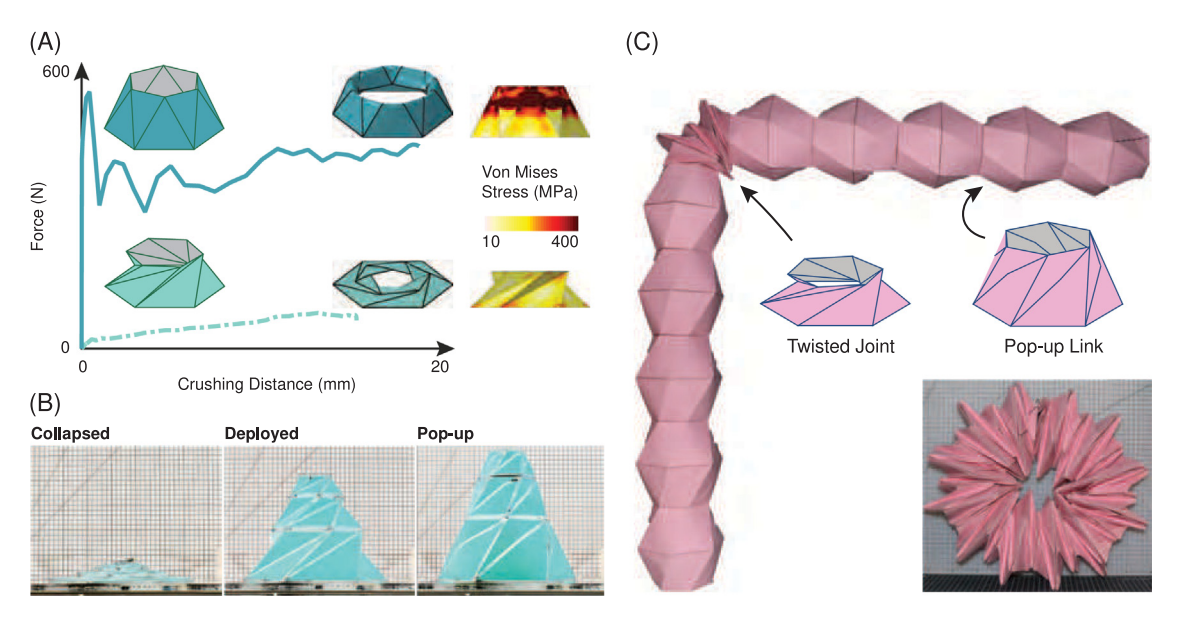


Fig. 7. Conceptual applications of Kresling corrugated tubes. (A) Tunable and deployable energy absorption system. The axial loading response is shown for the initial and pop-up frustum states, with the corresponding Von Mises stresses at the final crushed states. (B) Kresling frusta with decreasing radii are axially stacked to construct a deployable traffic cone that allows compact storage. (C) The different frusta of a reconfigurable robotic arm, can deform between the compliant mode and the stiff joint-link mode.

could explore modifications to the design where panels on one side of the polygonal frustum are made of thinner sheets such that they pop out at a lower pressure threshold. As shown in Fig. 3, the single-side pop out enables multi-stable rotation of the tube. By strategically placing the thinner side along the tube length, the tube can rotate towards various directions at different pressure levels. Additional studies could explore realization of these origami at a large scale where the thickness of panels would need to be accommodated, and creases would need to undergo large strains without failure. Finally, the pop-up stable state is likely not limited to the Kresling origami. A statistical model from a topological perspective would explore the relationship between different crease patterns and this type of pop-up behavior.

# **CRediT authorship contribution statement**

**Zhongyuan Wo:** Conceptualization, Methodology, Formulation, Implementation, Experimental realization, Figure visualization, Writing – original draft, Writing – review & editing. **Evgueni T. Filipov:** Conceptualization, Methodology, Resources, Writing – review & editing, Supervision, Funding acquisition.

# Declaration of competing interest

The authors declare that they have no known competing financial interests or personal relationships that could have appeared to influence the work reported in this paper.

# Data availability

Data will be made available on request.

# Acknowledgments

The authors acknowledge partial funding support from the Office of Naval Research, USA (Grant: N00014-20-5-B001 # 13209604), and the National Science Foundation, USA (Grant: CMMI #1943723). The paper reflects the views and opinions of the authors, and not necessarily those of the funding entities.

# Appendix A. Evaluating stiffness of the conical Kresling tube

# A.1. Definition of stiffness parameters in the bar and hinge model

In this work, we use a bar and hinge model to simulate the pop-up deformation and the subsequent behaviors. Mechanical stiffness and deformations of the origami structure are represented using a combination of three elements (Fig. A.1). The in-plane stiffness for stretching and shearing deformations are represented by space bar elements (Fig. A.1(B)). The out-of-plane bending stiffness of the sheet is lumped into discrete hinges that are placed along the diagonal of the quadrilateral (Fig. A.1(C)). Another type of hinge element, called the folding hinge, is placed along the crease to the capture stiffness related to folding the crease (Fig. A.1(D)). Each of those elements is assigned a stiffness that has been calibrated to the elastic material properties (Young's modulus E and Poisson's ratio  $\nu$ ), the sheet thickness t, as well as the panel geometries [51,53,54,69].

The in-plane stretching stiffness is represented by the space bar stiffness, which is a function of the material properties, the bar length, and the bar area. Formulations of bar cross-sectional areas for different polygonal panels have been established in the literature [51,69]. Our modeling strategy, however, involves subdivision of triangular panels in the conical Kresling, which require new bar area definitions for accuracy. Based on previous work, we modified the bar area definition such that the local (inplane stretching and shearing) and global (axial compression of a conical Kresling) behavior matches the result of finite-element simulation A.3. For a triangular panel of thickness t and polygonal area t, we assign an area t, for bar No. i belonging to this panel (Fig. A.1(B)):

$$A_i = \frac{0.36St}{(1-\nu)\sum w_i} \cdot \left(\frac{h_i}{w_i}\right)^{1/3} \tag{A.1}$$

where  $w_i$ ,  $h_i$  is the length and height corresponding to bar i. For a bar that intersects two triangles, its area is calculated by adding up the above values from both of the involved triangular panels.

The panel bending stiffness  $K_B$  depends on the material properties as well as the panel geometry. For a bending hinge of length

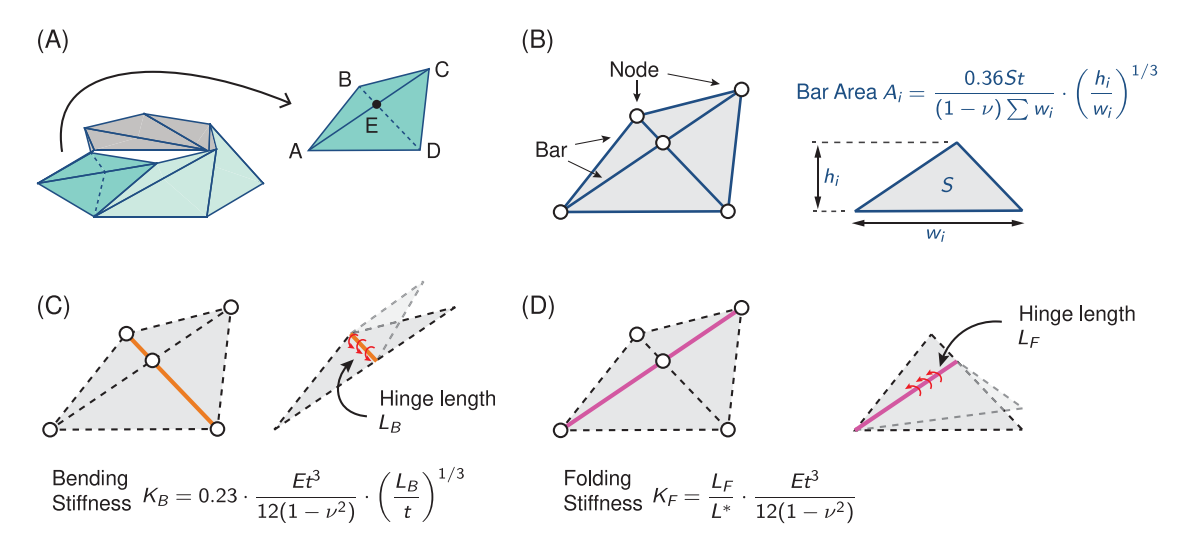


Fig. A.1. Stiffness definition of the bar and hinge model. (A) A frustum is discretized into bars and hinges. (B) The in-plane bars and the area definition. (C) The hinges for capturing the out-of-plane bending of the panels. (D) The hinges for representing the folding of the creases.

 $L_B$ , the stiffness definition is modified from previous work [51] in an effort to match the finite-element result of axial compression:

$$K_B = 0.23 \cdot \frac{Et^3}{12(1-\nu^2)} \cdot \left(\frac{L_B}{t}\right)^{1/3}$$
 (A.2)

The folding stiffness can be affected by case-specific factors and a precise description has not been established yet. As shown in Fig. A.1(D), for a crease line of length  $L_F$ , the stiffness is approximated by the following equation based on previous work [51,61]:

$$K_{F} = \frac{L_{F}}{L^{*}} \cdot \frac{Et^{3}}{12(1-\nu^{2})} \tag{A.3}$$

Complicated and localized effects such as the material anisotropy, fabrication process, and bending history, are simplified and reduced into a single parameter, called the length scale factor  $L^*$ . This factor is typically believed to be proportional to the sheet thickness [61]. Given that in our work the thickness t is normalized by the radius R to enable a scalable analysis,  $L^*$  is also normalized as  $L^*/R$  for a fully scalable analysis. In this work, we set  $L^*/R = 3$  unless specifically mentioned. Using a sensitivity analysis in the next section, we show that the value of  $L^*$  does not affect the qualitative results of the pop-up stability and the stiffness tuning.

# A.2. Energy calculation in the bar and hinge model

In this work, the stability type is determined by the landscape of the strain energy. In the bar and hinge model, the strain energy is separated into two parts: one stored in the bar elements ( $U_{\rm bar}$ ) and the other stored in the rotational hinges ( $U_{\rm spr}$ ).

For a bar element of length L, the bar area can be calculated using Eq. (A.1). Based on previous work [53], the stored energy of a bar element is then given by

$$U_{\rm bar} = WA \cdot L \tag{A.4}$$

In Eq. (A.4), W is the strain energy density given by

$$W = \sum_{i=1}^{N} \frac{\mu_j}{\alpha_j} \left( \lambda^{\alpha_j} - 3 \right) \tag{A.5}$$

where  $\lambda$  denotes the principal stretch, and N,  $\mu_j$ , and  $\alpha_j$  are the material constants. The principal stretch  $\lambda = \sqrt{2E_x + 1}$ , where  $E_x$  is the Green–Lagrange strain that can be calculated using the

nodal displacements of the bar element. Based on the aforementioned work, we select a special case with N=2. The material properties can be determined by providing  $\alpha_1=5,\ \alpha_2=1$  and setting the initial tangential modulus to be the Young's modulus.

For the rotational hinges, the strain energy is calculated as

$$U_{\rm spr} = \frac{1}{2} K_B (\varphi^B - \varphi_0^B)^2 + \frac{1}{2} K_F (\varphi^F - \varphi_0^F)^2$$
 (A.6)

where  $K_B$ ,  $K_F$  are the stiffness of the bending and folding hinges, respectively.  $\varphi^B \varphi^F$  denote the rotational angles of the bending and folding hinges, while the angles  $\varphi_0^B$ ,  $\varphi_0^F$  are the neutral angles at which the bending and folding springs are stress-free.

# A.3. Finite-element verifications

We perform finite-element simulations (ABAQUS/Standard [66]) on triangular panels and the origami frusta to verify the bar and hinge model. To examine the in-plane performance of the bar and hinge model, different triangular panels are stretched and sheared and compared to a similar simulation with a discretized FE model (Fig. A.2(A), B, D, and E). By varying the aspect ratio and the skew angle  $\beta$  (Fig. A.2(A)), the comparison can be made for triangular panels of various shapes. Fig. A.2(C) and F show the comparison, where the stiffness are normalized by the maximum value within each parametric range. For both of the characteristic deformation modes, the truss stiffness qualitatively match with the FE stiffness, while the error varies with the triangular shape. For less skewed triangles the bar and hinge model tends to underestimate the axial stiffness but overestimate the shear stiffness. For more skewed triangles ( $\sim \beta > 90^{\circ}$ ), the bar and hinge model is reasonably accurate for both stretching and shear deformations.

While the accuracy of the truss model for in-plane deformations does vary, typically the global response of most origami structures is determined by the geometry-dominated competition of kinematics and stiffness, not the localized material strains [52]. Thus, the global stiffness and the geometric influences could be predicted with reasonable accuracy even if the in-plane stiffness is only crudely approximated. In order to demonstrate this feature, we build a finite-element model of the origami frustum to provide a high-fidelity benchmark for the results (Fig. A.2G). Panels are meshed with S3 general purpose elements, where adjacent panels are connected via connector elements with prescribed stiffness to simulate crease rotations (the same stiffness as defined in Eq. (A.3)). Linear-elastic material properties are set to be

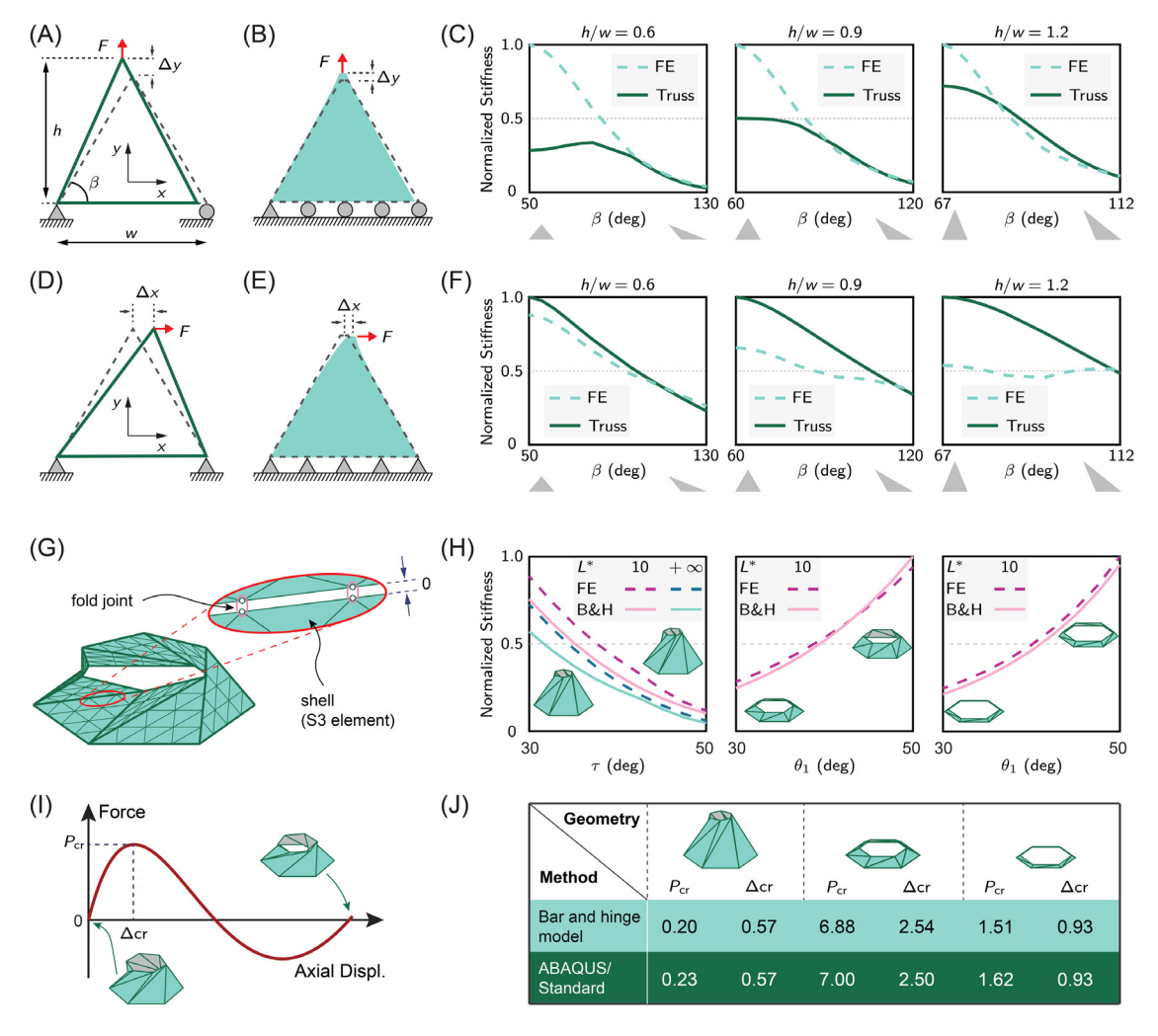


**Fig. A.2.** Comparison of the numerical predictions between the finite-element (FE) model and the bar and hinge model. In-plane deformations of triangular panels are simulated as stretching and shearing using the bar and hinge model (A, D) and the FE model (B, E), respectively. The normalized stiffness of stretching and shearing are shown in (C) and (F) for triangles of various shapes. (G) Finite-element model of the Kresling frustum shown with a representative sketch of the meshing scheme, while a finer mesh is used for the actual analyses. The zoom-in plot shows the details of the connections between adjacent panels. (H) Predictions of the axial stiffness of the frustum with the bar and hinge model and the FE model. (I) A sample bi-stable axial loading response of the frustum, where the critical force and the corresponding axial displacement are denoted by  $P_{CT}$  and  $\Delta_{CT}$ , respectively. (J) Predictions of  $P_{CT}$  and  $\Delta_{CT}$  with the bar and hinge model and the FE model.

the same as the bar and hinge model. Convergence with respect to the mesh density is examined, and a mesh size of roughly  $0.03R \times 0.03R$  can provide a stiffness estimation that is within 0.5% of a mesh with  $0.01R \times 0.01R$  elements. Aiming to minimize the discrepancy of the global axial stiffness, the calibration of the model returns the stretching and bending stiffness definitions as shown in Eq. (A.1)(A.2).

With the calibration, a close match of the axial stiffness is achieved for various geometries. In Fig. A.2H, we show the comparison for three categories of frusta. From left to right are frusta that would undergo twisting collapse, large-strain inversion, and small-strain inversion if the prescribed displacement is big enough. In each category, we vary either the twisting angle  $\tau$  or the slant angle  $\theta_1$  to enable a parametric comparison. The axial stiffness of the bar and hinge models are in good agreement with those of the FE models. Furthermore, we compare the large-displacement response between the bar and hinge model and the FE model. Specifically, the critical force and the associated axial displacement (Fig. A.2I), are computed using both numerical models. The results are listed in Fig. A.2J, and a good agreement is also achieved for the representative case from each of the above categories.

# A.4. Experimental proof-of-concept verification

# A.4.1. Sample fabrication

In this work, we fabricated physical models with different construction papers, and the normalized thickness is fixed at  $t/R=4\times10^{-3}$ . For the axial compression tests, the specimens are fabricated from paper sheets with a thickness of 0.25 mm, and the outer radius R is set to be 62 mm. For illustrating the multistable behaviors, however, we fabricate larger paper prototypes (R=93 mm) using thicker paper sheets (0.37 mm). For each frustum, the planar crease pattern is input into a CAD software and then cut into a paper sheet using a laser cutter (Universal Laser VLS6.60). The patterned sheet is then manually folded into the frustum shape. Each planar cut of the frustum has extra tabs for connecting them to neighboring units. For a stand-alone frustum, strips are attached to a hexagonal top and bottom edge that offers a similar confinement as that provided by an adjacent frustum.

We recognize that these physical models are made of paper and as such embody complexity that is not captured in our models, e.g., anisotropy [70]. However, the physical specimens are used primarily as a proof-of-concept verification to show that the types of multi-stable behavior observed in the simulations also occur in physical models with the same geometric parameters.

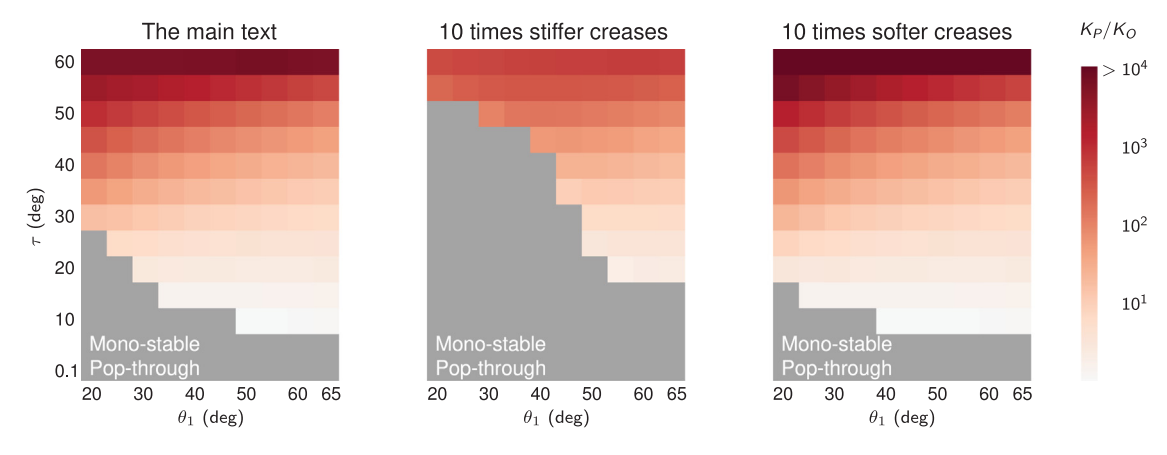
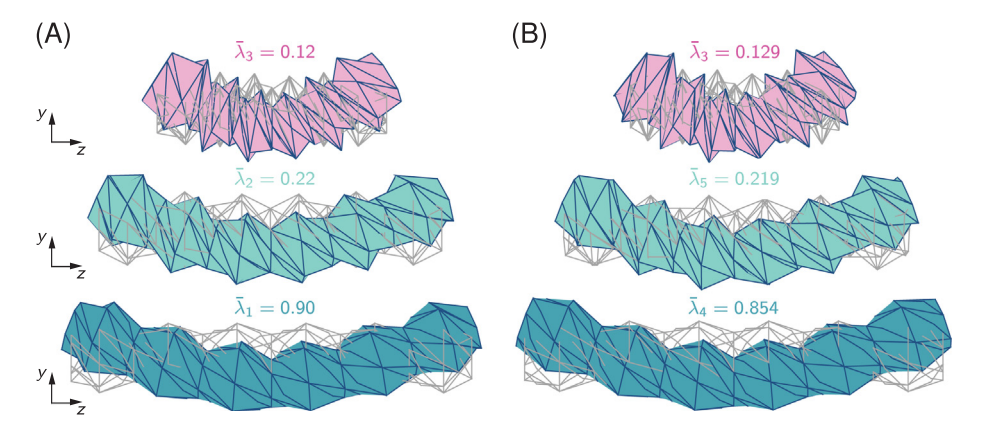


Fig. B.1. Sensitivity of the axial stiffness tuning with respect to the crease stiffness.



**Fig. B.2.** Reinforcing the ends of the tube prevents localized deformation modes but does not lead to a significant change in the bending eigenvalues. The deformation modes of global bending, as well as the normalized eigenvalues, are shown for tubes with (A) reinforced ends and (B) unreinforced ends. For the reinforced cases, the end frusta will not be popped or axially compressed. All eigenvalues are normalized by the maximum eigenvalue of the reinforced tube within the range of  $\tau \in [35^{\circ}, 55^{\circ}]$ .

# A.4.2. Setup of the axial compression test

In order to quantify the stiffness tunability experimentally, the frusta are loaded using a Mark-10 testing stand (ESM1500G) and a force gauge (M5-50). As shown in Fig. 4, the global compression strain (compression/frustum height) is controlled below 1% to avoid nonlinear effects. Each specimen is compressed at a strain rate of 1 mm/min. We observe that the axial compression response stabilizes after 20 load–unload cycles, thus every specimen is compressed 20 times prior to data collection.

# Appendix B. Sensitivity of the analyses

# B.1. Sensitivity of the stiffness tuning

In Section 4.1 of the main text, we show the axial stiffness of the frustum can be increased after the pop-up, with the magnitude increase primarily affected by the twisting angle  $\tau$ . A more twisted frustum will provide more significant stiffness tuning. Those results are collected with a user-defined crease stiffness  $L^*/R = 3$ , where in reality the actual  $L^*$  can vary depending on the type of origami structures. To investigate the effects of the case-specific  $L^*$  on the stiffness tuning, we perform a parametric study for three levels of crease stiffness (Fig. B.1). With stiffer creases, the bi-stable region shrinks, and the axial stiffness becomes less tunable (i.e., the stiffness ratios are smaller). This behavior is expected because folding energy has a negative impact on achieving bi-stable pop-up (Fig. 2(C)). Moreover, the axial stiffness of the initial state is mainly affected by the crease folding, whereas the

stiffness of the pop-up state is dominated by panels stretching and shearing. Therefore, stiffer creases only stiffen the initial state while have little effect on the pop-up state. The overall stiffness ratios thus become smaller. On the other hand, with softer creases, the bi-stable region expands and the stiffness ratios are greater. However, the value of crease stiffness does not change the trend of stiffness tuning of the overall findings reported earlier. A more twisted frustum still causes a more significant stiffness change, no matter what the crease stiffness is.

# B.2. Reinforcement of the tube ends

In Section 4.2, we study the global bending stiffness of tubes made of the Kresling frusta. In our study, we reinforce the end frusta of the tube to avoid eigenmodes that only involve local deformations. Specifically, we reinforce and stiffen the creases within the end frustum by 10<sup>4</sup> times to restrict the local deformations. This subsection verifies that this reinforcement does not substantially alter the global bending stiffness. Fig. B.2 shows the global bending eigenmodes and the normalized eigenvalues for both reinforced and unreinforced tubes at the three stable states. The eigenvalues are normalized by the maximum value within the range of  $\tau \in [35^{\circ}, 55^{\circ}]$  (see Fig. 6). Due to the reinforcement, the end frusta will not be popped or compressed when simulating the global bending of the pop-up tube and the twisted tube, respectively. With the reinforcement, the global bending is always mode # 3 for the twisted tube, # 2 for the initial tube, and # 1 for the pop-up tube (Fig. B.2(A)). The modes before the global bending correspond to flexible axial deformations.

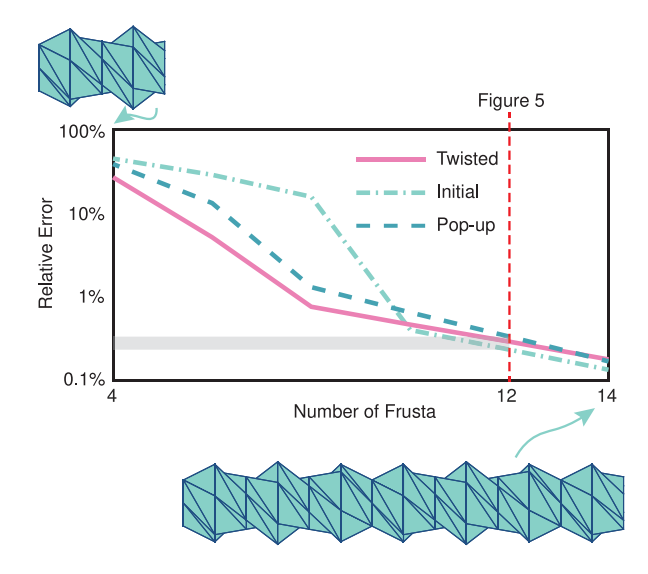


**Fig. B.3.** The estimated equivalent section modulus converges with the number of frusta. A tube with twenty frusta is used as a point of comparison to find the relative error. For the cantilever tests that are presented in Fig. 6, the relative errors are below 1%.

In Fig. B.2(B), we present the global bending eigenmodes for the corresponding tubes without the reinforcement. Notice that, now the global bending modes are 3, 5, 4 for the three states. Without the ends reinforcement, there exist some low-energy eigenmodes that only involve local deformations at the ends. In fact, the mode number of the global bending can vary for different geometries because of these local deformations. One must visually identify the bending eigenmode case by case, and manually collect the associated eigenvalue for the parametric analysis. The reinforcement at the ends allow us to automate this process, without bringing substantial differences into the eigenvalues. The relative error for the initial tube is lower than 0.5%, while the other states observe errors between 5% and 8%. For the reinforced tube, the twisted state is longer than the unreinforced counterpart because the end frusta are not compressed. As a consequence, the bending eigenvalue is smaller. On the other hand, for the pop-up state, the reinforced tube is shorter, and the bending eigenvalue is slightly greater than that of the unreinforced pop-up tube.

# B.3. Convergence of the equivalent section modulus with respect to the number of frusta used

In Section 4.2, the corrugated tubes are loaded as cantilevers at the three stable states. We calculate the equivalent section modulus based on this cantilever loading scenario, using a tube consisting of twelve identical frusta. Here, we show that, in the cantilever test, the twelve-frustum tube provides estimates of the section modulus that are within 1% of a twenty-frustum tube (Fig. B.3). This claim holds for all three stable states.

# References

- K. Bertoldi, V. Vitelli, J. Christensen, M. van Hecke, Flexible mechanical metamaterials, Nat. Rev. Mater. 2 (2017) 17066, http://dx.doi.org/10.1038/ natrevmats.2017.66.
- [2] Q. Zhong, J. Zhu, F.E. Fish, S.J. Kerr, A.M. Downs, H. Bart-Smith, D.B. Quinn, Tunable stiffness enables fast and efficient swimming in fish-like robots, Science Robotics 6 (57) (2021) eabe4088, http://dx.doi.org/10.1126/ scirobotics.abe4088.
- [3] M. Zhang, J. Yang, R. Zhu, Origami-based bistable metastructures for low-frequency vibration control, J. Appl. Mech. 88 (5) (2021) 051009, http://dx.doi.org/10.1115/1.4049953.

- [4] G. Sumbre, G. Fiorito, T. Flash, B. Hochner, Octopuses use a human-like strategy to control precise point-to-point arm movements, Curr. Biol. 16 (8) (2006) 767–772, http://dx.doi.org/10.1016/j.cub.2006.02.069.
- [5] Y.-J. Kim, S. Cheng, S. Kim, K. Iagnemma, A novel layer jamming mechanism with tunable stiffness capability for minimally invasive surgery, IEEE Trans. Robot. 29 (4) (2013) 1031–1042, http://dx.doi.org/10.1109/TRO. 2013.2256313.
- [6] S. Mintchev, J. Shintake, D. Floreano, Bioinspired dual-stiffness origami, Science Robotics 3 (20) (2018) http://dx.doi.org/10.1126/scirobotics. aau0275
- [7] B. Haghpanah, L. Salari-Sharif, P. Pourrajab, J. Hopkins, L. Valdevit, Multistable shape-reconfigurable architected materials, Adv. Mater. 28 (36) (2016) 7915–7920, http://dx.doi.org/10.1002/adma.201601650.
- [8] S. Li, K.W. Wang, Fluidic origami with embedded pressure dependent multi-stability: A plant inspired innovation, J. R. Soc. Interface 12 (111) (2015) http://dx.doi.org/10.1098/rsif.2015.0639.
- [9] F. Hongbin, C.S.-C. A., X. Yutong, W. Kon-Well, Programmable self-locking origami mechanical metamaterials, Adv. Mater. 30 (15) (2018) 1706311, http://dx.doi.org/10.1002/adma.201706311.
- [10] Y. Zhang, Q. Wang, M. Tichem, F. van Keulen, Design and characterization of multi-stable mechanical metastructures with level and tilted stable configurations, Extreme Mech. Lett. 34 (2020) 100593, http://dx.doi.org/ 10.1016/j.eml.2019.100593.
- [11] D. Vella, Buffering by buckling as a route for elastic deformation, Nat. Rev. Phys. 1 (7) (2019) 425–436, http://dx.doi.org/10.1038/s42254-019-0063-1.
- [12] D.M. Kochmann, K. Bertoldi, Exploiting microstructural instabilities in solids and structures: From metamaterials to structural transitions, Appl. Mech. Rev. 69 (5) (2017) 50801–50824, http://dx.doi.org/10.1115/ 1.4037966.
- [13] S. Shan, S.H. Kang, J.R. Raney, P. Wang, L. Fang, F. Candido, J.A. Lewis, K. Bertoldi, Multistable architected materials for trapping elastic strain energy, Adv. Mater. 27 (29) (2015) 4296–4301, http://dx.doi.org/10.1002/ adma.201501708.
- [14] D.P. Holmes, A.J. Crosby, Snapping surfaces, Adv. Mater. 19 (21) (2007) 3589–3593, http://dx.doi.org/10.1002/adma.200700584.
- [15] S. Janbaz, F.S.L. Bobbert, M.J. Mirzaali, A.A. Zadpoor, Ultra-programmable buckling-driven soft cellular mechanisms, Mater. Horiz. 6 (6) (2019) 1138–1147, http://dx.doi.org/10.1039/C9MH00125E.
- [16] Y. Zhang, D. Restrepo, M. Velay-Lizancos, N.D. Mankame, P.D. Zavattieri, Energy dissipation in functionally two-dimensional phase transforming cellular materials, Sci. Rep. 9 (1) (2019) 12581, http://dx.doi.org/10.1038/ s41598-019-48581-8.
- [17] Z. Yan, F. Zhang, F. Liu, M. Han, D. Ou, Y. Liu, Q. Lin, X. Guo, H. Fu, Z. Xie, M. Gao, Y. Huang, J. Kim, Y. Qiu, K. Nan, J. Kim, P. Gutruf, H. Luo, A. Zhao, K.-C. Hwang, Y. Huang, Y. Zhang, J.A. Rogers, Mechanical assembly of complex, 3D mesostructures from releasable multilayers of advanced materials, Sci. Adv. 2 (9) (2016) e1601014, http://dx.doi.org/10.1126/sciadv.1601014.
- [18] J.O. Almen, A. Laszlo, The uniform-section disc spring, Trans. ASME 58 (4) (1936) 305–314.
- [19] J.B. Friedman, Flexible drinking straw, 1951, U.S. Patent, May 1 1951.
- [20] Z. Wo, E.T. Filipov, Bending stability of corrugated tubes with anisotropic frustum shells, J. Appl. Mech. 89 (4) (2022) 041005, http://dx.doi.org/10. 1115/1.4053267.
- [21] F. Pan, Y. Li, Z. Li, J. Yang, B. Liu, Y. Chen, 3D pixel mechanical metamaterials, Adv. Mater. 31 (25) (2019) 1900548, http://dx.doi.org/10.1002/adma. 201900548.
- [22] Y. Liu, F. Pan, B. Ding, Y. Zhu, K. Yang, Y. Chen, Multistable shape-reconfigurable metawire in 3D space, Extreme Mech. Lett. 50 (2021) 101535, http://dx.doi.org/10.1016/j.eml.2021.101535.
- [23] A. Márquez, P.G. Fazzini, J.L. Otegui, Failure analysis of flexible metal hose at compressor discharge, Eng. Fail. Anal. 16 (6) (2009) 1912–1921, http://dx.doi.org/10.1016/j.engfailanal.2008.09.031.
- [24] F.C. Bardi, H. Tang, M. Kulkarni, X. Yin, Structural analysis of cryogenic flexible hose, in: Proceedings of the ASME 2011 30th International Conference on Ocean, Offshore and Arctic Engineering. Volume 3: Materials Technology; Jan Vugts Symposium on Design Methodology of Offshore Structures; Jo Pinkster Symposium on Second Order Wave Drift Forces, ASME, Rotterdam, The Netherlands, 2011, pp. 593–606, http://dx.doi.org/ 10.1115/OMAE2011-50238.
- [25] B. Ni, H. Gao, Engineer energy dissipation in 3D graphene nanolattice via reversible snap-through instability, J. Appl. Mech. 87 (3) (2019) http: //dx.doi.org/10.1115/1.4045544.
- [26] N.P. Bende, T. Yu, N.A. Corbin, M.A. Dias, C.D. Santangelo, J.A. Hanna, R.C. Hayward, Overcurvature induced multistability of linked conical frusta: How a 'bendy straw' holds its shape, Soft Matter 14 (42) (2018) 8636–8642, http://dx.doi.org/10.1039/C8SM01355A.
- [27] B. Zhang, Bistable and Multi-Stable Thin-Walled Structures (Ph.D. thesis), University of Oxford, Oxford, UK, 2017.
- [28] D. Ilssar, M. Pukshansky, Y. Or, A.D. Gat, Dynamics of reconfigurable straw-like elements, 2022, http://dx.doi.org/10.48550/ARXIV.2202.12657, arXiv.

- [29] E. Bernardes, S. Viollet, Design of an origami bendy straw for robotic multistable structures, J. Mech. Des. 144 (3) (2021) 033301, http://dx.doi. org/10.1115/1.4052222.
- [30] S. Li, H. Fang, S. Sadeghi, P. Bhovad, K.-W. Wang, Architected origami materials: How folding creates sophisticated mechanical properties, Adv. Mater. 31 (5) (2019) 1805282, http://dx.doi.org/10.1002/adma.201805282.
- [31] Z. Zhai, L. Wu, H. Jiang, Mechanical metamaterials based on origami and kirigami, Appl. Phys. Rev. 8 (4) (2021) 41319, http://dx.doi.org/10.1063/5. 0051088.
- [32] J.A. Faber, A.F. Arrieta, A.R. Studart, Bioinspired spring origami, Science 359 (6382) (2018) 1386–1391, http://dx.doi.org/10.1126/science.aap7753.
- [33] J.L. Silverberg, A.A. Evans, L. McLeod, R.C. Hayward, T. Hull, C.D. Santangelo, I. Cohen, Using origami design principles to fold reprogrammable mechanical metamaterials, Science 345 (6197) (2014) http://dx.doi.org/10.1126/science.1252876.
- [34] J.L. Silverberg, J.-H. Na, A.A. Evans, B. Liu, T.C. Hull, C.D. Santangelo, R.J. Lang, R.C. Hayward, I. Cohen, Origami structures with a critical transition to bistability arising from hidden degrees of freedom, Nat. Mater. 14 (4) (2015) 389–393, http://dx.doi.org/10.1038/nmat4232.
- [35] E.T. Filipov, M. Redoutey, Mechanical characteristics of the bistable origami hypar, Extreme Mech. Lett. 25 (2018) 16–26, http://dx.doi.org/10.1016/j. eml.2018.10.001.
- [36] J.-E. Suh, Y. Miyazawa, J. Yang, J.-H. Han, Self-reconfiguring and stiffening origami tube, Adv. Eng. Mater. 24 (5) (2022) 2101202, http://dx.doi.org/ 10.1002/adem.202101202.
- [37] S.D. Guest, S. Pellegrino, The folding of triangulated cylinders, Part I: Geometric considerations, J. Appl. Mech. 61 (4) (1994) 773–777, http://dx.doi.org/10.1115/1.2901553.
- [38] H. Yasuda, T. Tachi, M. Lee, J. Yang, Origami-based tunable truss structures for non-volatile mechanical memory operation, Nature Commun. 8 (1) (2017) 962, http://dx.doi.org/10.1038/s41467-017-00670-w.
- [39] S. Wu, Q. Ze, J. Dai, N. Udipi, G.H. Paulino, R. Zhao, Stretchable origami robotic arm with omnidirectional bending and twisting, Proc. Natl. Acad. Sci. 118 (36) (2021) e2110023118, http://dx.doi.org/10.1073/pnas. 2110023118
- [40] D. Melancon, A.E. Forte, L.M. Kamp, B. Gorissen, K. Bertoldi, Inflatable origami: Multimodal deformation via multistability, Adv. Funct. Mater. (2022) 2201891, http://dx.doi.org/10.1002/adfm.202201891.
- [41] A. Pagano, T. Yan, B. Chien, A. Wissa, S. Tawfick, A crawling robot driven by multi-stable origami, Smart Mater. Struct. 26 (9) (2017) 94007, http: //dx.doi.org/10.1088/1361-665x/aa721e.
- [42] P. Bhovad, J. Kaufmann, S. Li, Peristaltic locomotion without digital controllers: Exploiting multi-stability in origami to coordinate robotic motion, Extreme Mech. Lett. 32 (2019) 100552, http://dx.doi.org/10.1016/j.eml. 2019 100552
- [43] Q. Ze, S. Wu, J. Nishikawa, J. Dai, Y. Sun, S. Leanza, C. Zemelka, L.S. Novelino, G.H. Paulino, R.R. Zhao, Soft robotic origami crawler, Sci. Adv. 8 (13) (2022) eabm7834, http://dx.doi.org/10.1126/sciadv.abm7834.
- [44] J. Kaufmann, P. Bhovad, S. Li, Harnessing the multistability of kresling origami for reconfigurable articulation in soft robotic arms, Soft Robot. 9 (2) (2022) 212–223, http://dx.doi.org/10.1089/soro.2020.0075.
- [45] Z. Zhai, Y. Wang, H. Jiang, Origami-inspired, on-demand deployable and collapsible mechanical metamaterials with tunable stiffness, Proc. Natl. Acad. Sci. 115 (9) (2018) 2032–2037, http://dx.doi.org/10.1073/pnas. 1720171115.
- [46] L. Lu, X. Dang, F. Feng, P. Lv, H. Duan, Conical Kresling origami and its applications to curvature and energy programming, Proc. R. Soc. A 478 (2257) (2022) 20210712, http://dx.doi.org/10.1098/rspa.2021.0712.
- [47] S. Ishida, T. Nojima, I. Hagiwara, Mathematical approach to model foldable conical structures using conformal mapping, J. Mech. Des. 136 (9) (2014) 091007, http://dx.doi.org/10.1115/1.4027848.
- [48] T. Nojima, Development of foldable conical shell, Trans. Jpn. Soc. Mech. Eng. Ser. C 66 (647) (2000) 2463–2469, http://dx.doi.org/10.1299/kikaic. 66.2463
- [49] H. Sharma, S.H. Upadhyay, Geometric design and deployment behavior of origami inspired conical structures, Mech. Based Des. Struct. Mach. (2020) 1–25, http://dx.doi.org/10.1080/15397734.2020.1833738.

- [50] C. Jianguo, D. Xiaowei, Z. Ya, F. Jian, T. Yongming, Bistable behavior of the cylindrical origami structure with kresling pattern, J. Mech. Des. 137 (6) (2015) 061406, http://dx.doi.org/10.1115/1.4030158.
- [51] E.T. Filipov, K. Liu, T. Tachi, M. Schenk, G.H. Paulino, Bar and hinge models for scalable analysis of origami, Int. J. Solids Struct. 124 (2017) 26–45, http://dx.doi.org/10.1016/j.ijsolstr.2017.05.028.
- [52] M. Schenk, S.D. Guest, Origami folding: A structural engineering approach, in: P. Wang-Iverson, R.J. Lang, M. Yims (Eds.), Origami 5: Fifth International Meeting of Origami Science, Mathematics, and Education, CRC Press, New York, 2011, pp. 291–303.
- [53] K. Liu, G.H. Paulino, Nonlinear mechanics of non-rigid origami: An efficient computational approach, Proc. R. Soc. Lond. A 473 (2206) (2017) 20170348, http://dx.doi.org/10.1098/rspa.2017.0348.
- [54] S.R. Woodruff, E.T. Filipov, A bar and hinge model formulation for structural analysis of curved-crease origami, Int. J. Solids Struct. 204–205 (2020) 114–127, http://dx.doi.org/10.1016/j.ijsolstr.2020.08.010.
- [55] Y. Zhu, M. Schenk, E.T. Filipov, A review on origami simulations: From kinematics, to mechanics, toward multiphysics, Appl. Mech. Rev. 74 (3) (2022) 030801, http://dx.doi.org/10.1115/1.4055031.
- [56] E.D. Demaine, M.L. Demaine, V. Hart, G.N. Price, T. Tachi, (Non)existence of pleated folds: How paper folds between creases, Graphs Combin. 27 (3) (2011) 377–397, http://dx.doi.org/10.1007/s00373-011-1025-2.
- [57] B.A. DiDonna, T.A. Witten, Anomalous strength of membranes with elastic ridges, Phys. Rev. Lett. 87 (20) (2001) 206105, http://dx.doi.org/10.1103/ PhysRevLett 87 206105
- [58] A. Lobkovsky, S. Gentges, H. Li, D. Morse, T.A. Witten, Scaling properties of stretching ridges in a crumpled elastic sheet, Science 270 (5241) (1995) 1482–1485, http://dx.doi.org/10.1126/science.270.5241.1482.
- [59] T.A. Witten, Stress focusing in elastic sheets, Rev. Modern Phys. 79 (2) (2007) 643–675, http://dx.doi.org/10.1103/RevModPhys.79.643.
- [60] S. Borodulina, A. Kulachenko, M. Nygårds, S. Galland, Stress-strain curve of paper revisited, Nordic Pulp Pap. Res. J. 27 (2) (2012) 318–328, http: //dx.doi.org/10.3183/npprj-2012-27-02-p318-328.
- [61] F. Lechenault, B. Thiria, M. Adda-Bedia, Mechanical response of a creased sheet, Phys. Rev. Lett. 112 (24) (2014) 244301, http://dx.doi.org/10.1103/ PhysRevLett.112.244301.
- [62] C. Lauff, T.W. Simpson, M. Frecker, Z. Ounaies, S. Ahmed, P. von Lockette, R. Strzelec, R. Sheridan, J.-M. Lien, Differentiating bending from folding in origami engineering using active materials, in: Proceedings of the ASME 2014 International Design Engineering Technical Conferences & Computers and Information Engineering Conference. Volume 5B: 38th Mechanisms and Robotics Conference, Buffalo, New York, USA, 2014, http://dx.doi.org/ 10.1115/DETC2014-34702, V05BT08A040.
- [63] A. Giampieri, U. Perego, R. Borsari, A constitutive model for the mechanical response of the folding of creased paperboard, Int. J. Solids Struct. 48 (16) (2011) 2275–2287, http://dx.doi.org/10.1016/j.ijsolstr.2011.04.002.
- [64] L. Mentrasti, F. Cannella, M. Pupilli, J.S. Dai, Large bending behavior of creased paperboard. I. Experimental investigations, Int. J. Solids Struct. 50 (20) (2013) 3089–3096, http://dx.doi.org/10.1016/j.ijsolstr.2013.05.018.
- [65] Z. Wo, J.M. Raneses, E.T. Filipov, Locking zipper-coupled origami tubes for deployable energy absorption, J. Mech. Robot. 14 (4) (2022) 041007, http://dx.doi.org/10.1115/1.4054363.
- [66] ABAQUS, Abaqus FEA, Version 6.10 Documentation, Dassault Systemes Simulia Corp., Providence, RI. USA, 2010.
- [67] J. Ma, Z. You, Energy absorption of thin-walled square tubes with a prefolded origami pattern—Part I: Geometry and numerical simulation, J. Appl. Mech. 81 (1) (2013) 11003–11011, http://dx.doi.org/10.1115/1. 4024405
- [68] C. Laschi, B. Mazzolai, M. Cianchetti, Soft robotics: Technologies and systems pushing the boundaries of robot abilities, Science Robotics 1 (1) (2016) eaah3690, http://dx.doi.org/10.1126/scirobotics.aah3690.
- [69] K. Liu, G.H. Paulino, Highly efficient nonlinear structural analysis of origami assemblages using the MERLIN2 software, in: R.J. Lang (Ed.), Origami 7: Seventh International Meeting of Origami Science, Mathematics, and Education, vol. 4, Tarquin Group, St Albans, United Kingdom, 2018, pp. 1167–1182.
- [70] S.W. Grey, F. Scarpa, M. Schenk, Mechanics of paper-folded origami: A cautionary tale, Mech. Res. Commun. 107 (2020) 103540, http://dx.doi.org/ 10.1016/j.mechrescom.2020.103540.